

3

The seismic wave equation

Using the stress and strain theory developed in the previous chapter, we now construct and solve the seismic wave equation for elastic wave propagation in a uniform whole space. We will show that two types of solutions are possible, corresponding to compressional (P) and shear (S) waves, and we will derive the equations for their velocities that we presented in the last chapter. This will involve vector calculus and complex numbers; some of the mathematics is reviewed in Appendix B. For simplicity, in this chapter we assume perfect elasticity with no energy loss in the seismic waves from any intrinsic attenuation.

3.1 Introduction: The wave equation

To motivate our discussion, consider the one-dimensional wave equation

$$\frac{\partial^2 u}{\partial t^2} = c^2 \frac{\partial^2 u}{\partial x^2} \quad (3.1)$$

and its general solution

$$u(x, t) = f(x \pm ct), \quad (3.2)$$

which represents waves of arbitrary shape propagating at velocity c in the positive and negative x directions. This is a very common equation in physics and can be used to describe, for example, the vibrations of a string or acoustic waves in a pipe. The velocity of the wave is determined by the physical properties of the material through which it propagates. In the case of a vibrating string, $c^2 = F/\rho$ where F is the string tension force and ρ is the density.

The wave equation is classified as a *hyperbolic equation* in the theory of linear partial differential equations. Hyperbolic equations are among the most challenging to solve because sharp features in their solutions will persist and can reflect off boundaries. Unlike, for example, the diffusion equation, solutions will be smooth only if the initial conditions are smooth. This complicates both analytical and numerical solution methods.

As we shall see, the seismic wave equation is more complicated than equation (3.1) because it is three dimensional and the link between force and displacement involves the full stress–strain relationship for an elastic solid. However, the *P* and *S* seismic wave solutions share many characteristics with the solutions to the 1-D wave equation. They involve pulses of arbitrary shape that travel at speeds determined by the elastic properties and density of the medium, and these pulses are often decomposed into harmonic wave solutions involving sine and cosine functions. Stein and Wysession (2003, Section 2.2) provide a useful review of the 1-D wave equation as applied to a vibrating string, with analogies to seismic wave propagation in the Earth.

3.2 The momentum equation

In the previous chapter, the stress, strain, and displacement fields were considered in static equilibrium and unchanging with time. However, because seismic waves are time-dependent phenomena that involve velocities and accelerations, we need to account for the effect of momentum. We do this by applying Newton's law ($F = ma$ from your freshman physics class) to a continuous medium.

Consider the forces on an infinitesimal cube in an (x_1, x_2, x_3) coordinate system (Fig. 3.1). The forces on each surface of the cube are given by the product of the traction vector and the surface area. For example, the force on the plane normal to x_1 is given by

$$\begin{aligned} \mathbf{F}(\hat{\mathbf{x}}_1) &= \mathbf{t}(\hat{\mathbf{x}}_1) dx_2 dx_3 \\ &= \tau \hat{\mathbf{x}}_1 dx_2 dx_3 \\ &= \begin{bmatrix} \tau_{11} \\ \tau_{21} \\ \tau_{31} \end{bmatrix} dx_2 dx_3, \end{aligned} \tag{3.3}$$

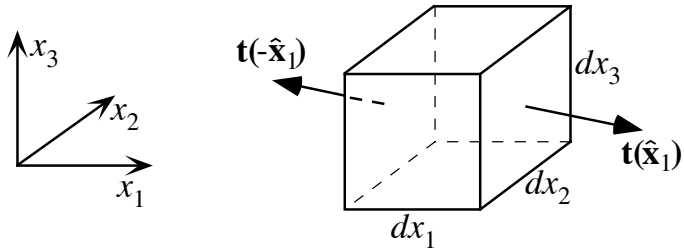


Figure 3.1 The force on the \$(x_2, x_3)\$ face of an infinitesimal cube is given by \$\mathbf{t}(\hat{\mathbf{x}}_1) dx_2 dx_3\$, the product of the traction vector and the surface area.

where \mathbf{F} is the force vector, \mathbf{t} is the traction vector, and $\boldsymbol{\tau}$ is the stress tensor. In the case of a homogeneous stress field, there is no net force on the cube since the forces on opposing sides will cancel out, that is, $\mathbf{F}(-\hat{\mathbf{x}}_1) = -\mathbf{F}(\hat{\mathbf{x}}_1)$. Net force will only be exerted on the cube if spatial gradients are present in the stress field. In this case, the net force from the planes normal to x_1 is

$$\mathbf{F}(\hat{\mathbf{x}}_1) = \frac{\partial}{\partial x_1} \begin{bmatrix} \tau_{11} \\ \tau_{21} \\ \tau_{31} \end{bmatrix} dx_1 dx_2 dx_3, \quad (3.4)$$

and we can use index notation and the summation convention to express the total force from the stress field on all the faces of the cube as

$$\begin{aligned} F_i &= \sum_{j=1}^3 \frac{\partial \tau_{ij}}{\partial x_j} dx_1 dx_2 dx_3 \\ &= \partial_j \tau_{ij} dx_1 dx_2 dx_3. \end{aligned} \quad (3.5)$$

The $d_j \tau_{ij}$ term is the divergence of the stress tensor (recall that the summation convention means that this term is summed over $j = 1, 2, 3$). There may also exist a body force on the cube that acts in proportion to the volume of material, that is,

$$F_i^{\text{body}} = f_i dx_1 dx_2 dx_3. \quad (3.6)$$

The mass of our infinitesimal cube is given by

$$m = \rho dx_1 dx_2 dx_3, \quad (3.7)$$

where ρ is the density. The acceleration of the cube is given by the second time derivative of the displacement \mathbf{u} . Substituting (3.5)–(3.7) into $F = ma$ and

cancelling the common factor of $dx_1 dx_2 dx_3$, we obtain¹

$$\rho \frac{\partial^2 u_i}{\partial t^2} = \partial_j \tau_{ij} + f_i. \quad (3.8)$$

This is the fundamental equation that underlies much of seismology. It is called the *momentum equation* or the *equation of motion* for a continuum. Each of the terms u_i , τ_{ij} , and f_i is a function of position \mathbf{x} and time. The body force term \mathbf{f} generally consists of a gravity term \mathbf{f}_g and a source term \mathbf{f}_s . Gravity is an important factor at very low frequencies in normal mode seismology, but it can generally be neglected for body- and surface-wave calculations at typically observed wavelengths. We will consider the effects of the source term \mathbf{f}_s later in this book (Chapter 9). In the absence of body forces, we have the *homogeneous equation of motion*

$$\rho \frac{\partial^2 u_i}{\partial t^2} = \partial_j \tau_{ij}, \quad (3.9)$$

which governs seismic wave propagation outside of seismic source regions. Generating solutions to (3.8) or (3.9) for realistic Earth models is an important part of seismology; such solutions provide the predicted ground motion at specific locations at some distance from the source and are commonly termed *synthetic seismograms*.

If, on the other hand, we assume that the acceleration term in (3.8) is zero, the result is the *static equilibrium equation*

$$\partial_j \tau_{ij} = -f_i. \quad (3.10)$$

in which the body forces are balanced by the divergence of the stress tensor. This equation is applicable to static deformation problems in geodesy, engineering, and many other fields.

3.3 The seismic wave equation

In order to solve (3.9) we require a relationship between stress and strain so that we can express $\boldsymbol{\tau}$ in terms of the displacement \mathbf{u} . Recall the linear, isotropic stress-strain

¹ In expressing the acceleration term, we approximate the *total* derivatives of \mathbf{u} with respect to time with the *partial* derivatives of \mathbf{u} with respect to time. That is, we make the small-deformation approximation such that the terms in the total derivative containing the spatial derivatives of \mathbf{u} can be ignored. This is generally assumed valid in seismology, but the spatial derivatives (advection terms) are very important in fluid mechanics.

relationship,

$$\tau_{ij} = \lambda \delta_{ij} e_{kk} + 2\mu e_{ij}, \quad (3.11)$$

where λ and μ are the Lamé parameters and the strain tensor is defined as

$$e_{ij} = \frac{1}{2}(\partial_i u_j + \partial_j u_i). \quad (3.12)$$

Substituting for e_{ij} in (3.11), we obtain

$$\tau_{ij} = \lambda \delta_{ij} \partial_k u_k + \mu (\partial_i u_j + \partial_j u_i). \quad (3.13)$$

Equations (3.9) and (3.13) provide a coupled set of equations for the displacement and stress. These equations are sometimes used directly at this point to model wave propagation in computer calculations by applying finite-difference techniques. In these methods, the stresses and displacements are computed at a series of grid points in the model, and the spatial and temporal derivatives are approximated through numerical differencing. The great advantage of finite-difference schemes is their relative simplicity and ability to handle Earth models of arbitrary complexity. However, they are extremely computationally intensive and do not necessarily provide physical insight regarding the behavior of the different wave types.

In the equations that follow, we will switch back and forth between vector notation and index notation. A brief review of vector calculus is given in Appendix B. If we substitute (3.13) into (3.9), we obtain

$$\begin{aligned} \rho \frac{\partial^2 u_i}{\partial t^2} &= \partial_j [\lambda \delta_{ij} \partial_k u_k + \mu (\partial_i u_j + \partial_j u_i)] \\ &= \partial_i \lambda \partial_k u_k + \lambda \partial_i \partial_k u_k + \partial_j \mu (\partial_i u_j + \partial_j u_i) + \mu \partial_j \partial_i u_j + \mu \partial_j \partial_j u_i \\ &= \partial_i \lambda \partial_k u_k + \partial_j \mu (\partial_i u_j + \partial_j u_i) + \lambda \partial_i \partial_k u_k + \mu \partial_i \partial_j u_j + \mu \partial_j \partial_i u_i. \end{aligned} \quad (3.14)$$

Defining $\ddot{\mathbf{u}} = \partial^2 \mathbf{u} / \partial t^2$, we can write this in vector notation as

$$\rho \ddot{\mathbf{u}} = \nabla \lambda (\nabla \cdot \mathbf{u}) + \nabla \mu \cdot [\nabla \mathbf{u} + (\nabla \mathbf{u})^T] + (\lambda + \mu) \nabla \nabla \cdot \mathbf{u} + \mu \nabla^2 \mathbf{u}. \quad (3.15)$$

We now use the vector identity

$$\nabla \times \nabla \times \mathbf{u} = \nabla \nabla \cdot \mathbf{u} - \nabla^2 \mathbf{u} \quad (3.16)$$

to change this to a more convenient form. We have

$$\nabla^2 \mathbf{u} = \nabla \nabla \cdot \mathbf{u} - \nabla \times \nabla \times \mathbf{u}. \quad (3.17)$$

Substituting this into (3.15), we obtain

$$\rho \ddot{\mathbf{u}} = \nabla \lambda (\nabla \cdot \mathbf{u}) + \nabla \mu \cdot [\nabla \mathbf{u} + (\nabla \mathbf{u})^T] + (\lambda + 2\mu) \nabla \nabla \cdot \mathbf{u} - \mu \nabla \times \nabla \times \mathbf{u}. \quad (3.18)$$

This is one form of the *seismic wave equation*. The first two terms on the right-hand side (r.h.s.) involve gradients in the Lamé parameters themselves and are non-zero whenever the material is inhomogeneous (i.e., contains velocity gradients). Most non-trivial Earth models for which we might wish to compute synthetic seismograms contain such gradients. However, including these factors makes the equations very complicated and difficult to solve efficiently. Thus, most practical synthetic seismogram methods ignore these terms, using one of two different approaches.

First, if velocity is only a function of depth, then the material can be modeled as a series of homogeneous layers. Within each layer, there are no gradients in the Lamé parameters and so these terms go to zero. The different solutions within each layer are linked by calculating the reflection and transmission coefficients for waves at both sides of the interface separating the layers. The effects of a continuous velocity gradient can be simulated by considering a “staircase” model with many thin layers. As the number of layers increases, these results can be shown to converge to the continuous gradient case (more layers are needed at higher frequencies). This approach forms the basis for many techniques for computing predicted seismic motions from one-dimensional Earth models; we will term these *homogeneous-layer methods*. They are particularly useful for studying surface waves and low- to medium-frequency body waves. However, at high frequencies they become relatively inefficient because large numbers of layers are necessary for accurate modeling.

Second, it can be shown that the strength of these gradient terms varies as $1/\omega$, where ω is frequency, and thus at high frequencies these terms will tend to zero. This approximation is made in most *ray-theoretical methods*, in which it is assumed that the frequencies are sufficiently high that the $1/\omega$ terms are unimportant. However, note that at any given frequency this approximation will break down if the velocity gradients in the material become steep enough. At velocity discontinuities between regions of shallow gradients, the approximation cannot be used directly, but the solutions above and below the discontinuities can be patched together through the use of reflection and transmission coefficients. The distinction between the homogeneous-layer and ray-theoretical approaches is often important and will be emphasized later in this book.

If we ignore the gradient terms, the momentum equation for homogeneous media becomes

$$\rho \ddot{\mathbf{u}} = (\lambda + 2\mu) \nabla \nabla \cdot \mathbf{u} - \mu \nabla \times \nabla \times \mathbf{u}. \quad (3.19)$$

This is a standard form for the seismic wave equation in homogeneous media and forms the basis for most body-wave synthetic seismogram methods. However, it is important to remember that it is an approximate expression, which has neglected the gravity and velocity gradient terms and has assumed a linear, isotropic Earth model.

We can separate this equation into solutions for *P* waves and *S* waves by taking the divergence and curl, respectively. Taking the divergence of (3.19) and using the vector identity $\nabla \cdot (\nabla \times \Psi) = 0$, we obtain:

$$\frac{\partial^2(\nabla \cdot \mathbf{u})}{\partial t^2} = \frac{\lambda + 2\mu}{\rho} \nabla^2(\nabla \cdot \mathbf{u}) \quad (3.20)$$

or

$$\nabla^2(\nabla \cdot \mathbf{u}) - \frac{1}{\alpha^2} \frac{\partial^2(\nabla \cdot \mathbf{u})}{\partial t^2} = 0, \quad (3.21)$$

where the *P*-wave velocity, α , is given by

$$\alpha^2 = \frac{\lambda + 2\mu}{\rho}. \quad (3.22)$$

Taking the curl of (3.19) and using the vector identity $\nabla \times (\nabla \phi) = 0$, we obtain:

$$\frac{\partial^2(\nabla \times \mathbf{u})}{\partial t^2} = -\frac{\mu}{\rho} \nabla \times \nabla \times (\nabla \times \mathbf{u}). \quad (3.23)$$

Using the vector identity (3.16) and $\nabla \cdot (\nabla \times \mathbf{u}) = 0$, this becomes

$$\frac{\partial^2(\nabla \times \mathbf{u})}{\partial t^2} = \frac{\mu}{\rho} \nabla^2(\nabla \times \mathbf{u}) \quad (3.24)$$

or

$$\nabla^2(\nabla \times \mathbf{u}) - \frac{1}{\beta^2} \frac{\partial^2(\nabla \times \mathbf{u})}{\partial t^2} = 0, \quad (3.25)$$

where the *S*-wave velocity, β , is given by

$$\beta^2 = \frac{\mu}{\rho}. \quad (3.26)$$

We can use (3.22) and (3.26) to rewrite the elastic wave equation (3.18) directly in terms of the *P* and *S* velocities:

$$\ddot{\mathbf{u}} = \alpha^2 \nabla \nabla \cdot \mathbf{u} - \beta^2 \nabla \times \nabla \times \mathbf{u}. \quad (3.27)$$

3.3.1 Potentials

The displacement \mathbf{u} is often expressed in terms of the P -wave scalar potential ϕ and S -wave vector potential Ψ , using the Helmholtz decomposition theorem (e.g., Aki and Richards, 2002, pp. 67–9), i.e.,

$$\mathbf{u} = \nabla\phi + \nabla \times \Psi, \quad \nabla \cdot \Psi = 0. \quad (3.28)$$

We then have

$$\nabla \cdot \mathbf{u} = \nabla^2\phi \quad (3.29)$$

and

$$\begin{aligned} \nabla \times \mathbf{u} &= \nabla \times \nabla \times \Psi \\ &= \nabla \nabla \cdot \Psi - \nabla^2 \Psi \quad (\text{from 3.16}) \\ &= -\nabla^2 \Psi \quad (\text{since } \nabla \cdot \Psi = 0). \end{aligned} \quad (3.30)$$

Motivated by (3.21) and (3.25), we require that these potentials also satisfy

$$\nabla^2\phi - \frac{1}{\alpha^2} \frac{\partial^2\phi}{\partial t^2} = 0, \quad (3.31)$$

$$\nabla^2\Psi - \frac{1}{\beta^2} \frac{\partial^2\Psi}{\partial t^2} = 0. \quad (3.32)$$

After solving these equations for ϕ and Ψ , the P -wave displacement is given by the gradient of ϕ and the S -wave displacement is given by the curl of Ψ , following (3.28).

3.4 Plane waves

At this point it is helpful to introduce the concept of a *plane wave*. This is a solution to the wave equation in which the displacement varies only in the direction of wave propagation and is constant in the directions orthogonal to the propagation direction. For example, for a plane wave traveling along the x axis, the displacement may be expressed as

$$\mathbf{u}(x, t) = \mathbf{f}(t \pm x/c), \quad (3.33)$$

where c is the velocity of the wave, \mathbf{f} is any arbitrary function (a vector function is required to express the polarization of the wave), and the waves are propagating in

Table 3.1: Harmonic wave parameters.

Angular frequency	ω	time $^{-1}$	$\omega = 2\pi f = \frac{2\pi}{T} = ck$
Frequency	f	time $^{-1}$	$f = \frac{\omega}{2\pi} = \frac{1}{T} = \frac{c}{\Lambda}$
Period	T	time	$T = \frac{1}{f} = \frac{2\pi}{\omega} = \frac{\Lambda}{c}$
Velocity	c	distance time $^{-1}$	$c = \frac{\Lambda}{T} = f\Lambda = \frac{\omega}{k}$
Wavelength	Λ	distance	$\Lambda = \frac{c}{f} = cT = \frac{2\pi}{k}$
Wavenumber	k	distance $^{-1}$	$k = \frac{\omega}{c} = \frac{2\pi}{\Lambda} = \frac{2\pi f}{c} = \frac{2\pi}{cT}$

either the $+x$ or $-x$ direction. The displacement does not vary with y or z ; the wave extends to infinity in these directions. If $\mathbf{f}(t)$ is a discrete pulse, then u assumes the form of a displacement pulse traveling as a planar wavefront. More generally, displacement at position vector \mathbf{x} for a plane wave propagating in the unit direction $\hat{\mathbf{s}}$ may be expressed as

$$\mathbf{u}(\mathbf{x}, t) = \mathbf{f}(t - \hat{\mathbf{s}} \cdot \mathbf{x}/c) \quad (3.34)$$

$$= \mathbf{f}(t - \mathbf{s} \cdot \mathbf{x}), \quad (3.35)$$

where $\mathbf{s} = \hat{\mathbf{s}}/c$ is the *slowness vector*, whose magnitude is the reciprocal of the velocity.

Since seismic energy is usually radiated from localized sources, seismic wavefronts are always curved to some extent; however, at sufficiently large distances from the source the wavefront becomes flat enough that a plane wave approximation becomes locally valid. Furthermore, many techniques for solving the seismic wave equation involve expressing the complete solution as a sum of plane waves of differing propagation angles. Often the time dependence is also removed from the equations by transforming into the frequency domain. In this case the displacement for a particular angular frequency ω may be expressed as

$$\mathbf{u}(\mathbf{x}, t) = \mathbf{A}(\omega) e^{-i\omega(t-\mathbf{s}\cdot\mathbf{x})} \quad (3.36)$$

$$= \mathbf{A}(\omega) e^{-i(\omega t - \mathbf{k}\cdot\mathbf{x})}, \quad (3.37)$$

where $\mathbf{k} = \omega\mathbf{s} = (\omega/c)\hat{\mathbf{s}}$ is termed the *wavenumber vector*. We will use complex numbers to represent harmonic waves throughout this book; details of how this works are reviewed in Appendix B. This may be termed a *monochromatic* plane wave; it is also sometimes called the *harmonic* or *steady-state* plane wave solution. Other parameters used to describe such a wave are the wavenumber $k = |\mathbf{k}| = \omega/c$, the frequency $f = \omega/(2\pi)$, the period $T = 1/f$, and the wavelength $\Lambda = cT$. Equations relating the various harmonic wave parameters are summarized in Table 3.1.

3.4.1 Example: Harmonic plane wave equation

What is the equation for the displacement of a 1 Hz P -wave propagating in the $+x$ direction at 6 km/s? In this case $\omega = 2\pi f$, where $f = 1$ Hz, and thus $\omega = 2\pi$. The slowness vector is in the direction of the x axis and thus $\hat{\mathbf{s}} = \hat{\mathbf{x}} = (1, 0, 0)$ and $\mathbf{s} = (1/c, 0, 0) = (1/6, 0, 0)$ s/km. We can thus express (3.36) as

$$\mathbf{u}(\mathbf{x}, t) = \mathbf{u}(x, t) = \mathbf{A}e^{-2i\pi(t-x/6)}$$

where t is in s and x is in km. As we shall see in the next section, P waves are polarized in the direction of wave propagation, so $\mathbf{u} = (u_x, 0, 0)$ and we can express this more simply as

$$u_x(x, t) = A e^{-2i\pi(t-x/6)}.$$

In general, the coefficient A is complex to permit any desired phase at $x = 0$. As described in Appendix B, the real part must be taken for this equation to have a physical meaning. An alternative form is

$$u_x(x, t) = a \cos [2\pi(t - x/6) - \phi]$$

where a is the amplitude and ϕ is the phase at $x = 0$ (see Figure B.3).

3.5 Polarizations of P and S waves

Consider plane P waves propagating in the x direction. From (3.31) we have

$$\alpha^2 \partial_{xx} \phi = \partial_{tt} \phi. \quad (3.38)$$

A general solution to (3.38) can be written as

$$\phi = \phi_0(t \pm x/\alpha), \quad (3.39)$$

where a minus sign corresponds to propagation in the $+x$ direction and a plus sign denotes propagation in the $-x$ direction. Because $\mathbf{u} = \nabla \phi$, we have

$$\begin{aligned} u_x &= \partial_x \phi, \\ u_y &= 0, \\ u_z &= 0. \end{aligned} \quad (3.40)$$

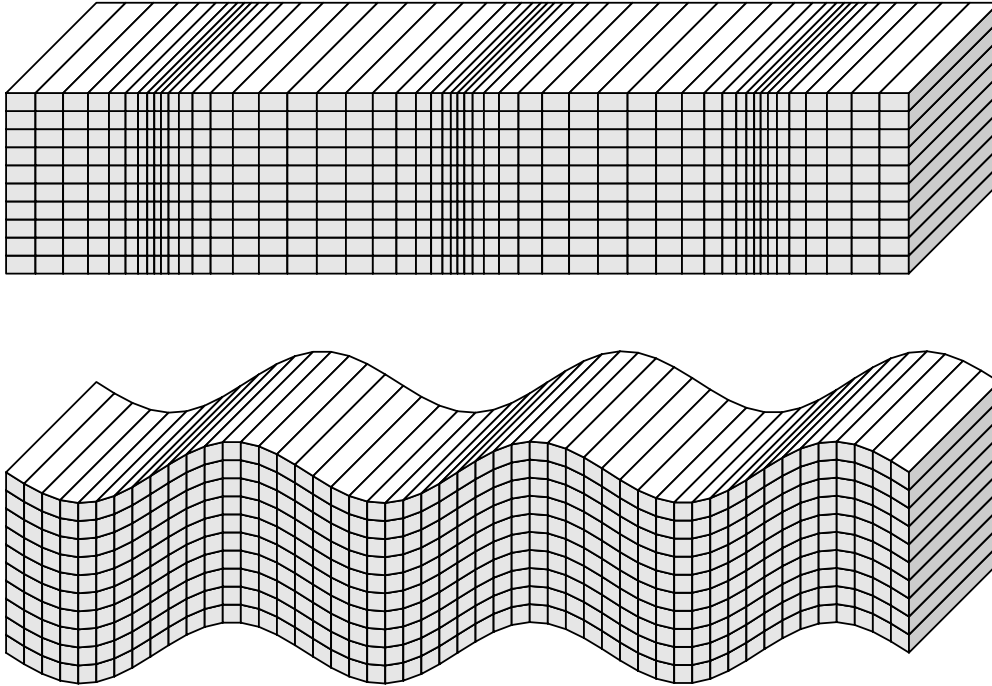


Figure 3.2 Displacements occurring from a harmonic plane *P* wave (top) and *S* wave (bottom) traveling horizontally across the page. *S*-wave propagation is pure shear with no volume change, whereas *P* waves involve both a volume change and shearing (change in shape) in the material. Strains are highly exaggerated compared to actual seismic strains in the Earth.

Note that for a plane wave propagating in the x direction there is no change in the y and z directions, and so the spatial derivatives ∂_y and ∂_z are zero. For *P* waves, the only displacement occurs in the direction of propagation along the x axis. Such wave motion is termed “longitudinal.” Also, because $\nabla \times \nabla\phi = 0$, the motion is curl-free or “irrotational.” Since *P* waves introduce volume changes in the material ($\nabla \cdot \mathbf{u} \neq 0$), they can also be termed “compressional” or “dilatational.” However, note that *P* waves involve shearing as well as compression; this is why the *P* velocity is sensitive to both the bulk and shear moduli. Particle motion for a harmonic *P* wave is shown in Figure 3.2.

Now consider a plane *S* wave propagating in the positive x direction. The vector potential becomes

$$\Psi = \Psi_x(t - x/\beta)\hat{\mathbf{x}} + \Psi_y(t - x/\beta)\hat{\mathbf{y}} + \Psi_z(t - x/\beta)\hat{\mathbf{z}}. \quad (3.41)$$

The displacement is

$$\begin{aligned} u_x &= (\nabla \times \Psi)_x = \partial_y \Psi_z - \partial_z \Psi_y = 0, \\ u_y &= (\nabla \times \Psi)_y = \partial_z \Psi_x - \partial_x \Psi_z = -\partial_x \Psi_z, \\ u_z &= (\nabla \times \Psi)_z = \partial_x \Psi_y - \partial_y \Psi_x = \partial_x \Psi_y, \end{aligned} \quad (3.42)$$

where again we have used $\partial_y = \partial_z = 0$, thus giving

$$\mathbf{u} = -\partial_x \Psi_z \hat{\mathbf{y}} + \partial_x \Psi_y \hat{\mathbf{z}}. \quad (3.43)$$

The motion is in the y and z directions, perpendicular to the propagation direction. S-wave particle motion is often divided into two components: the motion within a vertical plane through the propagation vector (*SV* waves) and the horizontal motion in the direction perpendicular to this plane (*SH* waves). Because $\nabla \cdot \mathbf{u} = \nabla \cdot (\nabla \times \Psi) = 0$, the motion is pure shear without any volume change (hence the name shear waves). Particle motion for a harmonic shear wave polarized in the vertical direction (*SV* wave) is illustrated in Figure 3.2.

3.6 Spherical waves

Another solution to the scalar wave equation (3.31) for the *P*-wave potential ϕ is possible if we assume spherical symmetry. In spherical coordinates, the Laplacian operator is

$$\nabla^2 \phi(r) = \frac{1}{r^2} \frac{\partial}{\partial r} \left[r^2 \frac{\partial \phi}{\partial r} \right], \quad (3.44)$$

where we have dropped the angular derivatives because of the spherical symmetry. Using this expression in (3.31), we have

$$\frac{1}{r^2} \frac{\partial}{\partial r} \left[r^2 \frac{\partial \phi}{\partial r} \right] - \frac{1}{\alpha^2} \frac{\partial^2 \phi}{\partial t^2} = 0. \quad (3.45)$$

Solutions to this equation outside the point $r = 0$ may be expressed as

$$\phi(r, t) = \frac{f(t \pm r/\alpha)}{r}. \quad (3.46)$$

Note that this is identical to the plane wave equation (3.33), except for the factor of $1/r$. Inward and outward propagating waves are specified by the $+$ and $-$ signs respectively. Since this expression is usually used to model waves radiating away from a point source, the inward propagating solution is normally ignored. In this case the $1/r$ term represents a decay in the wave amplitude with range, a geometrical spreading factor that we will explore further in Chapter 6.

Equation (3.46) is not a valid solution to (3.45) at $r = 0$. However, it can be shown (e.g., Aki and Richards, 2002, Section 4.1) that (3.46) is the solution to the

inhomogeneous wave equation

$$\nabla^2 \phi(r) - \frac{1}{\alpha^2} \frac{\partial^2 \phi}{\partial t^2} = -4\pi \delta(r) f(t), \quad (3.47)$$

where the delta function $\delta(r)$ is zero everywhere except $r = 0$ and has a volume integral of 1. The factor $4\pi \delta(r) f(t)$ represents the source-time function at the origin. We will return to this equation when we discuss seismic source theory in Chapter 9.

9

Earthquakes and source theory

In the preceding chapters we have described methods for modeling the propagation of seismic waves, but we have largely neglected the question of where the waves come from and how the radiated seismic energy relates to the physical properties of the source. These topics can often be ignored if our interest is solely in learning about details of Earth structure outside of the source regions, such as travel time studies of velocity structure. However, in many cases resolving seismic structure requires some knowledge of the source characteristics, and, of course, resolving source properties is fundamental to any real understanding of earthquakes. Because seismic source theory can be very complex, we will not formally derive most of the equations in this chapter; instead we will summarize many of the important results that are of practical use in seismology and refer the reader to Aki and Richards (2002), Stein and Wysession (2002), or Kanamori and Brodsky (2004) for more details.

9.1 Green's functions and the moment tensor

A major goal in this chapter is to understand how the observed seismic displacements at some distance from a seismic event can be related to the source properties. Let us begin by recalling the momentum equation for an elastic continuum

$$\rho \frac{\partial^2 u_i}{\partial t^2} = \partial_j \tau_{ij} + f_i, \quad (9.1)$$

where ρ is the density, u_i is the displacement, τ_{ij} is the stress tensor, and f_i is the body force term. Now consider the displacement field in a volume V bounded by a surface S . The displacements within V must be a function solely of the initial conditions, the internal forces within V , and the tractions acting on S . A more

formal statement of this fact is termed the *uniqueness* or *representation* theorem and is derived in Section 2.3 of Aki and Richards (2002). It turns out that specifying either the tractions or the displacement field on S , together with the body forces \mathbf{f} , is sufficient to uniquely determine \mathbf{u} throughout V .

Solving (9.1) in general is quite difficult if we include the f_i term, and in Chapter 3 we quickly dropped it to concentrate on the homogeneous equation of motion. Let us now explore how the properties of the source can be modeled and related to the seismic displacements observed in the Earth. Consider a unit force vector $\mathbf{f}(\mathbf{x}_0, t_0)$ applied at point \mathbf{x}_0 at time t_0 . By itself, this is not a realistic seismic source; rather, it is what would result if the hand of God could reach inside the Earth and apply a push to a particular point. Nonetheless, the unit force function is a useful concept because more realistic sources can be described as a sum of these force vectors. Consider the displacement $\mathbf{u}(\mathbf{x}, t)$ measured at a receiver at position \mathbf{x} that results from this source. In general, $\mathbf{u}(\mathbf{x}, t)$ will be a complicated function of the Earth's seismic velocity and density structure and will include multiple seismic phases and reverberations. The $\mathbf{u}(t)$ function will vary for different source and receiver positions. However, for every $\mathbf{f}(\mathbf{x}_0, t_0)$ and \mathbf{x} , there is a unique $\mathbf{u}(t)$ that describes the Earth's response, which could be computed if we knew the Earth's structure to sufficient accuracy.

In considering this problem, it is helpful to develop a notation that separates the source terms from all the other details of the wave propagation. This is done by defining a Green's function $\mathbf{G}(\mathbf{x}, t)$ that gives the displacement at point \mathbf{x} that results from the unit force function applied at point \mathbf{x}_0 . In general we may write

$$u_i(\mathbf{x}, t) = G_{ij}(\mathbf{x}, t; \mathbf{x}_0, t_0) f_j(\mathbf{x}_0, t_0), \quad (9.2)$$

where \mathbf{u} is the displacement, \mathbf{f} is the force vector, and \mathbf{G} is termed the elastodynamic Green's function. The actual computation of \mathbf{G} is quite complicated and involves taking into account all of the elastic properties of the material and the appropriate boundary conditions, and we defer discussion of specific forms for \mathbf{G} until later. However, assuming that \mathbf{G} can be computed, notice the power of this equation. Because it is linear, the displacement resulting from any body-force distribution can be computed as the sum or *superposition* of the solutions for the individual point sources. It also implies that knowledge of the displacement field may permit us to invert for the body-force distribution.

An earthquake is usually modeled as slip on a fault, a discontinuity in displacement across an internal surface in the elastic media. This parameterization cannot be used directly in (9.2) to model ground motion. Fortunately, however, it can be shown that there exists a distribution of body forces that produces exactly the same displacement field as slip on an internal fault. These are termed the *equivalent body*

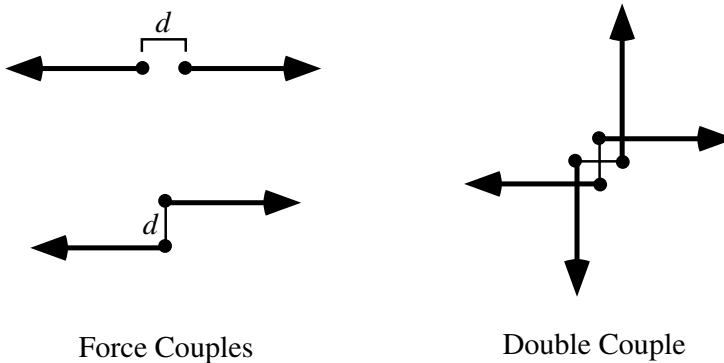


Figure 9.1 Force couples are opposing point forces separated by a small distance. A double couple is a pair of complementary couples that produce no net torque.

forces for the fault model. Before describing the relationship between these forces and the fault slip, let us first explore the different types of body forces that can occur within Earth.

For now, consider sources small enough compared to the wavelength of the radiated energy that they can be thought of as point sources. A single force acting at a point could only result from external forces; otherwise momentum would not be conserved. Internal forces resulting from an explosion or stress release on a fault must act in opposing directions so as to conserve momentum. For example, we could have two force vectors of magnitude f , pointing in opposite directions, separated by a distance d (Fig. 9.1). This is termed a *force couple* or *vector dipole*. Alternatively, the vectors could be separated in a direction perpendicular to the force orientation. In this case angular momentum is not conserved unless there also exists a complementary couple that balances the forces. The resulting pair of couples is termed a *double couple*.

We define the force couple M_{ij} in a Cartesian coordinate system as a pair of opposing forces pointing in the i direction, separated in the j direction. The nine different force couples are shown¹ in Figure 9.2.

The magnitude of M_{ij} is given by the product fd and is assumed constant as d goes to zero in the limit of a point source. It is then natural to define the *moment tensor* \mathbf{M} as

$$\mathbf{M} = \begin{bmatrix} M_{11} & M_{12} & M_{13} \\ M_{21} & M_{22} & M_{23} \\ M_{31} & M_{32} & M_{33} \end{bmatrix}. \quad (9.3)$$

¹ Alert readers will notice that our coordinate system has flipped again, so that x_3 points upward as it did in Chapters 2 and 3, rather than downward as it did in Chapters 4–8. An upward pointing x_3 axis is the usual convention in source studies.

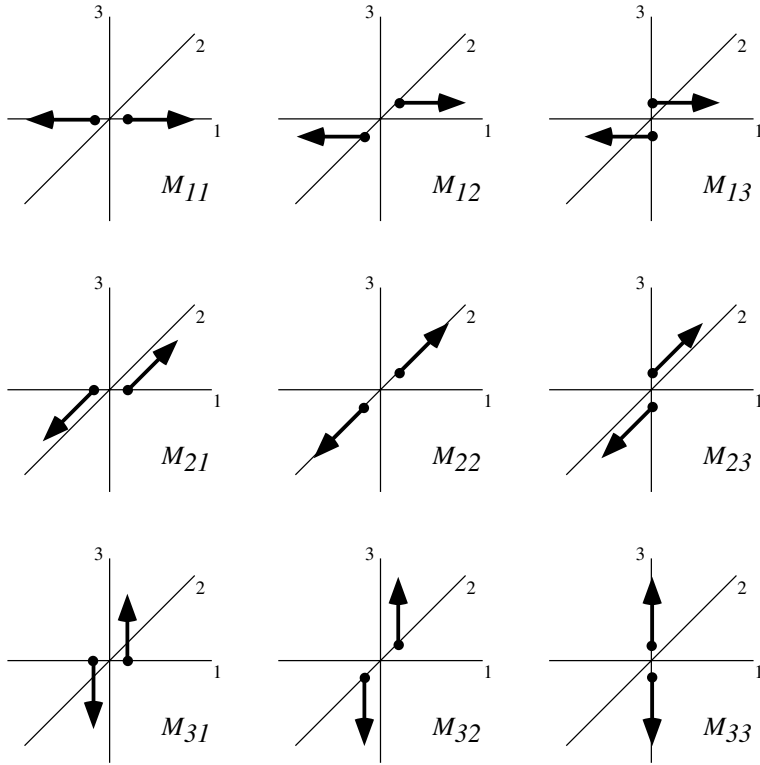


Figure 9.2 The nine different force couples that make up the components of the moment tensor.

The condition that angular momentum be conserved requires that \mathbf{M} is symmetric (e.g., that $M_{ij} = M_{ji}$). Therefore \mathbf{M} has only six independent elements. The moment tensor provides a general representation of the internally generated forces that can act at a point in an elastic medium. Although it is an idealization, it has proven to be a good approximation for modeling the distant seismic response for sources that are small compared with the observed seismic wavelengths. Larger, more complicated sources can also be modeled using the moment tensor representation by considering a sum of point forces at different positions.

Using (9.2), we may express the displacement resulting from a force couple at \mathbf{x}_0 in terms of the point-force Green's function as

$$\begin{aligned} u_i(\mathbf{x}, t) &= G_{ij}(\mathbf{x}, t; \mathbf{x}_0, t_0) f_j(\mathbf{x}_0, t_0) - G_{ij}(\mathbf{x}, t; \mathbf{x}_0 - \hat{\mathbf{x}}_k d, t_0) f_j(\mathbf{x}_0, t_0) \\ &= \frac{\partial G_{ij}(\mathbf{x}, t; \mathbf{x}_0, t_0)}{\partial (x_0)_k} f_j(\mathbf{x}_0, t_0) d, \end{aligned} \quad (9.4)$$

where the force vectors f_j are separated by a distance d in the $\hat{\mathbf{x}}_k$ direction. The product $f_j d$ is the k th column of M_{jk} and thus

$$u_i(\mathbf{x}, t) = \frac{\partial G_{ij}(\mathbf{x}, t; \mathbf{x}_0, t_0)}{\partial (x_0)_k} M_{jk}(\mathbf{x}_0, t_0), \quad (9.5)$$

and we see that there is a linear relationship between the displacement and the components of the moment tensor that involves the spatial derivatives of the point-force Green's functions. The synthetic seismogram algorithms discussed in Chapter 3 can be used to calculate the Green's functions, which include all the body- and surface-wave phases connecting \mathbf{x}_0 and \mathbf{x} . Given a specified moment tensor, source location and Earth model, it is possible to compute displacement functions (i.e., seismograms) anywhere within the Earth. Because (9.5) is linear, once the Green's functions are computed for a reference Earth model, it is straightforward to use seismic observations, $\mathbf{u}(\mathbf{x}, t)$, to invert for the components of the moment tensor. This is now done routinely for globally recorded earthquakes by several groups. The most widely used moment tensor catalog is from the Global Centroid Moment Tensor (CMT) project (see <http://www.globalcmt.org/CMTsearch.html>). This project was started by Adam Dziewonski and for many years was called the Harvard CMT catalog (e.g., Dziewonski and Woodhouse, 1983). The CMT solution provides the moment tensor and also a *centroid* time and position that represents the average time/space origin of the long-period seismic radiation. The centroid location should not be confused with the earthquake hypocenter, which is usually determined from short-period P arrival times and which represents the starting point of the earthquake rupture.

9.2 Earthquake faults

Let us now consider models of slip on earthquake faults and how they relate to the moment tensor formalism that we have just discussed. Earthquakes may be idealized as movement across a planar fault of arbitrary orientation (Fig. 9.3). The fault plane is defined by its *strike* (ϕ , the azimuth of the fault from north where it intersects a horizontal surface) and *dip* (δ , the angle from the horizontal). For non-vertical faults, the lower block is termed the *foot wall*; the upper block is the *hanging wall*. The slip vector is defined by the movement of the hanging wall relative to the foot wall; the *rake*, λ , is the angle between the slip vector and the strike. Upward movement of the hanging wall is termed *reverse* faulting, whereas downward movement is called *normal* faulting. Reverse faulting on faults with dip angles less than 45° is also called *thrust* faulting; nearly horizontal thrust faults are termed *overthrust* faults. In general, reverse faults involve horizontal compression in the direction perpendicular to the fault strike whereas normal faults involve horizontal extension. Horizontal motion between the fault surfaces is termed strike-slip and vertical motion is called dip-slip. If an observer, standing on one side of a fault, sees the adjacent block move to the right, this is termed *right-lateral* strike-slip motion (with the reverse indicating *left-lateral* motion). To define the rake for

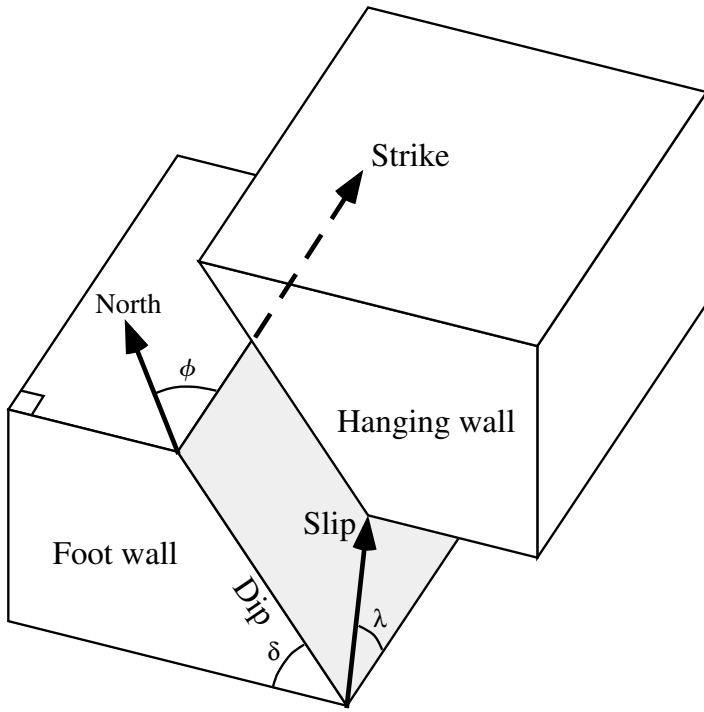


Figure 9.3 A planar fault is defined by the strike and dip of the fault surface and the direction of the slip vector.

vertical faults, the hanging wall is assumed to be on the right for an observer looking in the strike direction. In this case, $\lambda = 0^\circ$ for a left-lateral fault and $\lambda = 180^\circ$ for a right-lateral fault. The San Andreas Fault is a famous example of a right-lateral fault. Parts of California to the west of the fault are moving northward (right) relative to the rest of the United States.

The strike ($0 \leq \phi < 360^\circ$), the dip ($0 \leq \delta \leq 90^\circ$), the rake ($0 \leq \lambda < 360^\circ$), and the magnitude of the slip vector, D , define the most basic seismic model of faulting or event *focal mechanism*. It can be shown that the seismic energy radiated from such a fault can be modeled with a double-couple source, the equivalent body-force representation of the displacement field. For example, right-lateral movement on a vertical fault oriented in the x_1 direction corresponds to the moment tensor representation

$$\mathbf{M} = \begin{bmatrix} 0 & M_0 & 0 \\ M_0 & 0 & 0 \\ 0 & 0 & 0 \end{bmatrix}, \quad (9.6)$$

where M_0 is defined as the *scalar seismic moment* and is given by

$$M_0 = \mu \bar{D} A, \quad (9.7)$$

where μ is the shear modulus, \overline{D} is the average fault displacement, and A is the area of the fault. Scalar seismic moment was defined by Aki (1966) and is the most fundamental and widely used measure of earthquake strength. The reader should verify that the units for M_0 are N m, the same as for the force couples defined earlier.² More generally, M_0 can be computed from any moment tensor from

$$M_0 = \frac{1}{\sqrt{2}} \left(\sum_{ij} M_{ij}^2 \right)^{1/2}. \quad (9.8)$$

The connection between scalar moment as defined in (9.7) and the components of the moment tensor is complicated to prove (e.g., Aki and Richards, 2002, pp. 42–8), but is one of the most important results in seismology because it relates a real, physical property of the earthquake source to the double-couple model and ultimately to seismic observations. From the orientations of the different force couples, it is easy to see how any fault in which the strike, dip, and rake are multiples of 90° can be defined with a moment tensor representation. However, more generally, a fault plane and slip of any orientation can be described with a suitable rotation of the moment tensor in (9.6). Because $M_{ij} = M_{ji}$, there are two fault planes that correspond to a double-couple model. For example, (9.6) is also appropriate for a left-lateral strike-slip fault oriented in the x_2 direction (Fig. 9.4). Both faults have

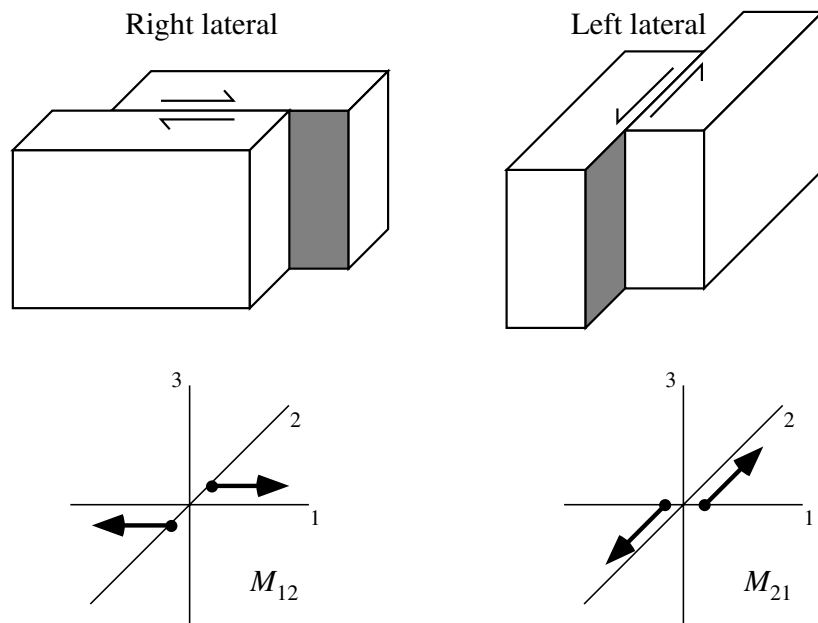


Figure 9.4 Owing to the symmetry of the moment tensor, these right-lateral and left-lateral faults have the same moment tensor representation and the same seismic radiation pattern.

² Older references sometimes express M_0 in dyne-cm. Note that $1 \text{ N} = 10^5 \text{ dyne}$ and thus $1 \text{ Nm} = 10^7 \text{ dyne-cm}$.

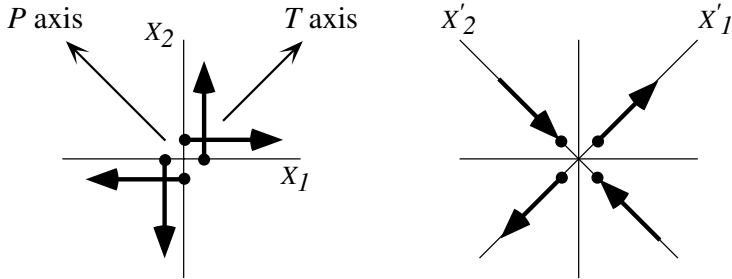


Figure 9.5 The double-couple pair on the left is represented by the off-diagonal terms in the moment tensor, M_{12} and M_{21} . By rotating the coordinate system to align with the P and T axes, the moment tensor in the new coordinate system is diagonal with opposing M_{11} and M_{22} terms.

the same moment tensor representation. This is a fundamental ambiguity in inverting seismic observations for fault models. In general, there are two fault planes that are consistent with distant seismic observations in the double-couple model. The real fault plane is termed the *primary fault plane*; the other is termed the *auxiliary fault plane*. This ambiguity is not a defect of the double-couple model (which has been shown to provide an excellent match to seismic observations) but reflects the fact that both faults produce exactly the same seismic displacements in the far field. Distinguishing between the primary and auxiliary fault planes requires examination of factors that go beyond a point source model (e.g., considering different parts of the rupture plane) or use of other information, such as aftershock locations or observed surface rupture.

Because the moment tensor is symmetric, it can be diagonalized by computing its eigenvalues and eigenvectors and rotating to a new coordinate system (just as we did for the stress and strain tensors in Chapter 2). For the example moment tensor given in (9.6), the principal axes are at 45° to the original x_1 and x_2 axes (Fig. 9.5), and the rotated moment tensor becomes

$$\mathbf{M}' = \begin{bmatrix} M_0 & 0 & 0 \\ 0 & -M_0 & 0 \\ 0 & 0 & 0 \end{bmatrix}. \quad (9.9)$$

The x'_1 coordinate is termed the *tension axis*, T , and x'_2 is called the *pressure axis*, P . The two sets of force couples plotted in Figure 9.5 are equivalent; they have the same moment tensor representation and they produce the same seismic radiation.

9.2.1 Non-double-couple sources

Double-couple sources arising from shear fracture have a specific moment tensor representation, in which both the trace and determinant of \mathbf{M} are zero. However, the moment tensor is a more general description of possible sources than double-

couple sources alone, and moment tensors computed from seismic data may include contributions from other types of events. The trace of the moment tensor is a measure of volume changes that accompany the event and is always zero for simple shear sources. In contrast, the moment tensor for an isotropic source (e.g., an explosion) has the form

$$\mathbf{M} = \begin{bmatrix} M_{11} & 0 & 0 \\ 0 & M_{22} & 0 \\ 0 & 0 & M_{33} \end{bmatrix}, \quad (9.10)$$

where $M_{11} = M_{22} = M_{33}$.

From a general moment tensor, we can extract the isotropic part as

$$\mathbf{M}^0 = \frac{1}{3}(\text{tr } \mathbf{M})\mathbf{I} \quad (9.11)$$

and decompose \mathbf{M} into isotropic and deviatoric parts:

$$\mathbf{M} = \mathbf{M}^0 + \mathbf{M}' \quad (9.12)$$

where $\text{tr } \mathbf{M}' = 0$. The deviatoric moment tensor, \mathbf{M}' , is free of any isotropic sources but may contain additional non-double-couple components. We can diagonalize \mathbf{M}' by computing its eigenvalues and eigenvectors and rotating to coordinates defined by its principal axes. We then have

$$\mathbf{M}' = \begin{bmatrix} \sigma_1 & 0 & 0 \\ 0 & \sigma_2 & 0 \\ 0 & 0 & \sigma_3 \end{bmatrix}, \quad (9.13)$$

where the eigenvalues are ordered such that $\sigma_1 > \sigma_2 > \sigma_3$. Because $\text{tr } \mathbf{M}' = 0$, we also have $\sigma_2 = -\sigma_1 - \sigma_3$. For a pure double-couple source, $\sigma_2 = 0$ and $\sigma_3 = -\sigma_1$. Following Knopoff and Randall (1970) we can further decompose \mathbf{M}' into a best-fitting double-couple, \mathbf{M}^{DC} , and a second term called a *compensated linear vector dipole*, \mathbf{M}^{CLVD}

$$\begin{aligned} \mathbf{M}' &= \mathbf{M}^{\text{DC}} + \mathbf{M}^{\text{CLVD}} \\ &= \begin{bmatrix} \frac{1}{2}(\sigma_1 - \sigma_3) & 0 & 0 \\ 0 & 0 & 0 \\ 0 & 0 & -\frac{1}{2}(\sigma_1 - \sigma_3) \end{bmatrix} + \begin{bmatrix} -\sigma_2/2 & 0 & 0 \\ 0 & \sigma_2 & 0 \\ 0 & 0 & -\sigma_2/2 \end{bmatrix}. \end{aligned} \quad (9.14)$$

The complete decomposition of the original \mathbf{M} is thus

$$\mathbf{M} = \mathbf{M}^0 + \mathbf{M}^{\text{DC}} + \mathbf{M}^{\text{CLVD}}. \quad (9.15)$$

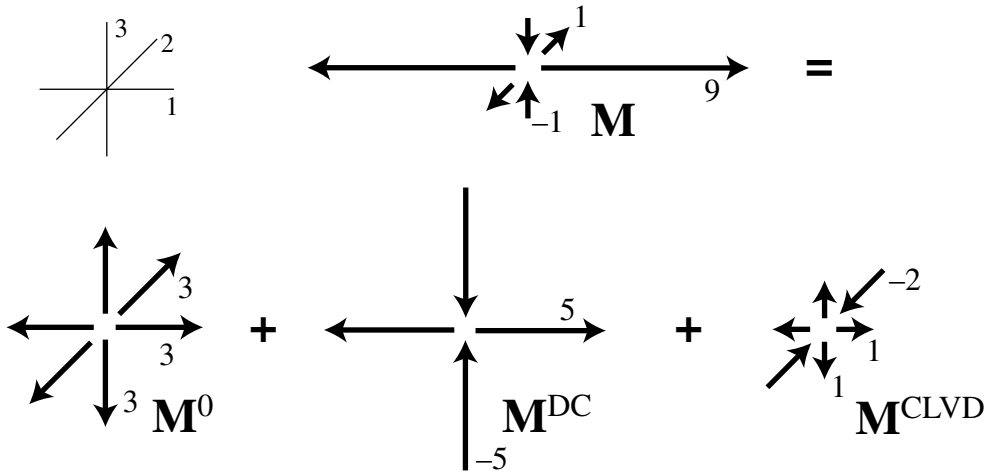


Figure 9.6 Example of the decomposition of a moment tensor into isotropic, best-fitting double couple, and compensated linear vector dipole terms.

Note that the decomposition of \mathbf{M}' into \mathbf{M}^{DC} and \mathbf{M}^{CLVD} is unique only because we have defined \mathbf{M}^{DC} as the *best-fitting* double-couple source, that is, we have minimized the CLVD part. There are alternative decompositions that will give a larger CLVD component and a correspondingly smaller double-couple moment tensor. Here is an example of the separation of a moment tensor into the components in (9.15), assuming it has already been rotated into its principal axes coordinates:

$$\mathbf{M} = \begin{bmatrix} 9 & 0 & 0 \\ 0 & 1 & 0 \\ 0 & 0 & -1 \end{bmatrix} = \begin{bmatrix} 3 & 0 & 0 \\ 0 & 3 & 0 \\ 0 & 0 & 3 \end{bmatrix} + \begin{bmatrix} 5 & 0 & 0 \\ 0 & 0 & 0 \\ 0 & 0 & -5 \end{bmatrix} + \begin{bmatrix} 1 & 0 & 0 \\ 0 & -2 & 0 \\ 0 & 0 & 1 \end{bmatrix}$$

as displayed in Figure 9.6. Alternatively, \mathbf{M}' can be decomposed into two double-couple sources

$$\mathbf{M}' = \begin{bmatrix} \sigma_1 & 0 & 0 \\ 0 & \sigma_2 & 0 \\ 0 & 0 & \sigma_3 \end{bmatrix} = \begin{bmatrix} \sigma_1 & 0 & 0 \\ 0 & -\sigma_1 & 0 \\ 0 & 0 & 0 \end{bmatrix} + \begin{bmatrix} 0 & 0 & 0 \\ 0 & -\sigma_3 & 0 \\ 0 & 0 & \sigma_3 \end{bmatrix}, \quad (9.16)$$

where we have used $\sigma_2 = -\sigma_1 - \sigma_3$. The larger and smaller of the two terms are called the *major* and *minor* double couples, respectively. This decomposition has the peculiar property that the major and minor double couples become nearly equal in size as σ_2 approaches zero; thus in most cases the decomposition of (9.15) is preferred.

Most earthquakes are well-described with double-couple sources, but the search for possible non-double-couple contributions has been a significant area of research (e.g., see reviews by Julian *et al.*, 1998, and Miller *et al.*, 1998). At one time it was hypothesized that deep focus earthquakes might involve volume changes caused by

sudden implosive phase changes in minerals within the subducting slabs. However, results have generally indicated that these events do not have significant isotropic components (e.g., Kawakatsu, 1991). Moment tensor inversions will sometimes impose the constraint that \mathbf{M} is purely deviatoric; this reduces the number of free parameters and can often lead to more stable results. A measure of the misfit between \mathbf{M}' and a pure double-couple source is provided by the ratio of σ_2 to the remaining eigenvalue with the largest magnitude

$$\epsilon = \sigma_2 / \max(|\sigma_1|, |\sigma_3|), \quad (9.17)$$

where $\epsilon = 0$ is obtained for a pure double-couple and $\epsilon = \pm 0.5$ is obtained for a pure compensated linear vector dipole.

Physically, non-double-couple components can arise from simultaneous faulting on faults of different orientations or on a curved fault surface. For example, CMT solutions for some Iceland earthquakes near Bardarbunga volcano suggest reverse faulting on outward dipping cone-shaped faults associated with caldera structures (Nettles and Ekström, 1998). Magma injection events can cause both isotropic and compensated linear vector dipole terms. For example, Kanamori *et al.* (1993) identified a dominant CLVD source for a 1984 earthquake near Tori Shima island in the Izu-Bonin arc. Perhaps the most exotic sources of all are volcanic eruptions (e.g., Kanamori *et al.*, 1984), landslides, such as Mt. St. Helens (Kanamori and Given, 1982), and glacial sliding events, such as the Greenland quakes recently discovered by Ekström *et al.* (2003). Seismic data from these events cannot be fit with standard force couples and moment tensor analysis and require single force models.

9.3 Radiation patterns and beach balls

To use the equivalent body-force representation to predict displacements, we need to know the elastodynamic Green's function, \mathbf{G} , in (9.2). In general, solving for \mathbf{G} is rather complicated. However, some insight into the nature of the solutions that are obtained may be found by considering the simple case of a spherical wavefront from an isotropic source. In Chapter 3, we described how the solution for the P -wave potential in this case is given by

$$\phi(r, t) = \frac{-f(t - r/\alpha)}{r}, \quad (9.18)$$

where α is the P velocity, r is the distance from the point source, and $4\pi\delta(r)f(t)$ is the source-time function. Note that the amplitude of the potential diminishes as $1/r$,

as we derived earlier from geometrical spreading considerations for a spherical wavefront. The displacement field is given by the gradient of the displacement potential

$$u(r, t) = \frac{\partial \phi(r, t)}{\partial r} = \left(\frac{1}{r^2} \right) f(t - r/\alpha) - \left(\frac{1}{r} \right) \frac{\partial f(t - r/\alpha)}{\partial r}. \quad (9.19)$$

Defining $\tau = t - r/\alpha$ as the *delay time*, where r/α is the time that it takes a P wave to travel the distance r from the source, we have

$$\frac{\partial f(t - r/\alpha)}{\partial r} = \frac{\partial f(t - r/\alpha)}{\partial \tau} \frac{\partial \tau}{\partial r} = -\frac{1}{\alpha} \frac{\partial f(t - r/\alpha)}{\partial \tau},$$

and so (9.19) can be expressed as

$$u(r, t) = \left(\frac{1}{r^2} \right) f(t - r/\alpha) + \left(\frac{1}{r\alpha} \right) \frac{\partial f(t - r/\alpha)}{\partial \tau}. \quad (9.20)$$

This equation is relatively simple because it applies only to P waves and involves no radiation pattern effects as the source is assumed to be spherically symmetric. The first term decays as $1/r^2$ and is called the *near-field term* since it is important only relatively close to the source. It represents the permanent static displacement due to the source. The second term decays as $1/r$ and is called the *far-field term* because it will become dominant at large distances from the source. It represents the dynamic response – the transient seismic waves that are radiated by the source that cause no permanent displacement. These waves have displacements that are given by the first time derivative of the source-time function.

More complicated expressions arise for point force and double-couple sources, but these also involve near- and far-field terms. Most seismic observations are made at sufficient distance from faults that only the far-field terms are important. The far-field P -wave displacement from the jk component of a moment tensor source at $\mathbf{x} = 0$ in a homogeneous whole space is given by

$$u_i^P(\mathbf{x}, t) = \frac{1}{4\pi\rho\alpha^3} \frac{x_i x_j x_k}{r^3} \frac{1}{r} \dot{M}_{jk} \left(t - \frac{r}{\alpha} \right), \quad (9.21)$$

where $r^2 = x_1^2 + x_2^2 + x_3^2$ is the squared distance to the receiver and \dot{M} is the time derivative of the moment tensor. This is a general expression that gives the far-field P displacements for any moment tensor representation of the source.

Now let us consider the more specific example of a fault described by a double-couple source. Without loss of generality we may assume that the fault is in the $(x_1,$

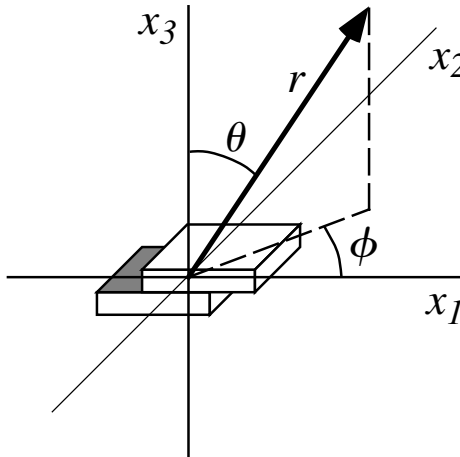


Figure 9.7 Spherical coordinates for a vector relative to a fault in the (x_1, x_2) plane with slip in the x_1 direction.

x_2) plane with motion in the x_1 direction (Fig. 9.7). We then have $M_{13} = M_{31} = M_0$ and

$$u_i^P(\mathbf{x}, t) = \frac{1}{2\pi\rho\alpha^3} \frac{x_i x_1 x_3}{r^3} \frac{1}{r} \dot{M}_0 \left(t - \frac{r}{\alpha} \right). \quad (9.22)$$

Note that the factor of two difference from (9.21) is due to the sum over M_{13} and M_{31} . If we define spherical coordinates relative to the fault as shown in Figure 9.7, we have

$$\begin{aligned} x_3/r &= \cos \theta, \\ x_1/r &= \sin \theta \cos \phi, \\ x_i/r &= \hat{r}_i, \end{aligned} \quad (9.23)$$

and thus, substituting for x in (9.22) and using $\cos \theta \sin \theta = \frac{1}{2} \sin 2\theta$, we have

$$\mathbf{u}^P = \frac{1}{4\pi\rho\alpha^3} \sin 2\theta \cos \phi \frac{1}{r} \dot{M}_0 \left(t - \frac{r}{\alpha} \right) \hat{\mathbf{r}}. \quad (9.24)$$

The P -wave radiation pattern is illustrated in Figure 9.8. Note that the fault plane and the auxiliary fault plane (the plane perpendicular to the fault plane and the slip vector) form nodal lines of zero motion that separate the P -wave polarities into four quadrants. The outward pointing vectors represent outward P -wave displacement in the far field (assuming \dot{M} is positive); this is termed the compressional quadrant. The inward pointing vectors occur in the dilatational quadrant. The tension (T axis) is in the middle of the compressional quadrant; the pressure (P axis) is in the middle of the dilatational quadrant. (Yes, it's confusing! The *tension* axis is in the

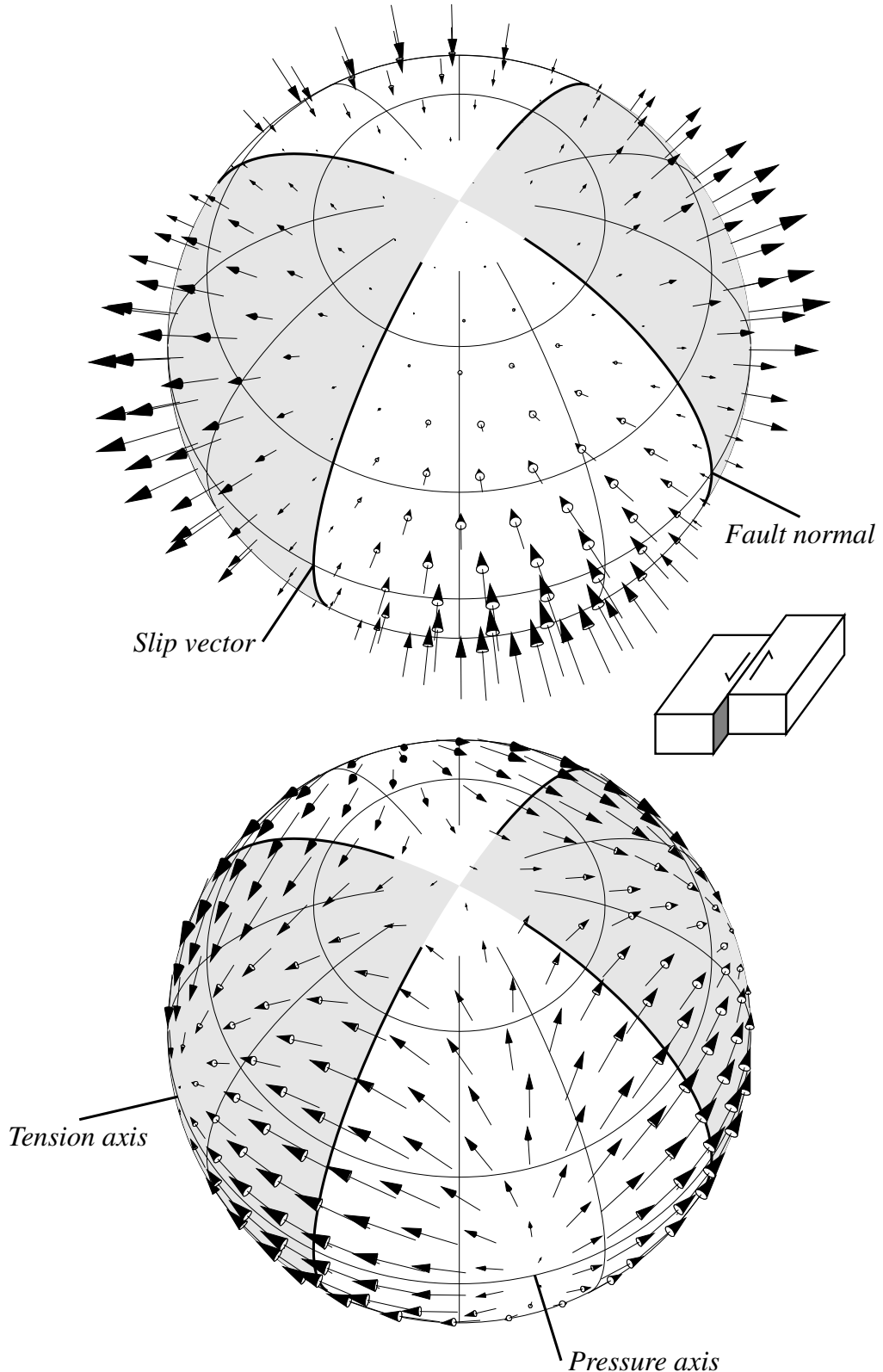


Figure 9.8 The far-field radiation pattern for P waves (top) and S waves (bottom) for a double-couple source. The orientation of the small arrows shows the direction of first motion; their length is proportional to the wave amplitude. The primary and auxiliary fault planes are shown as heavy lines; the compressional quadrants are shaded. P -wave first motions are outward in the compressional quadrant and inward in the dilatational quadrant with nodal lines in between. S -wave first motions are generally away from the pressure axis and toward the tension axis; there are six nodal points and no nodal lines in S . Because of the ambiguity between the primary and auxiliary fault planes, the positions of the slip and fault normal vectors in the top plot could be reversed.

compressional quadrant; compressional in this case refers to the outward direction of P first motion.)

For S waves the equations are only slightly more complicated. The far-field S displacements as a function of M_{jk} are given by

$$u_i^S(\mathbf{x}, t) = \frac{(\delta_{ij} - \gamma_i \gamma_j) \gamma_k}{4\pi\rho\beta^3} \frac{1}{r} \dot{M}_{jk} \left(t - \frac{r}{\beta} \right), \quad (9.25)$$

where β is the shear velocity and the direction cosines are $\gamma_i = x_i/r$. For a double-couple source with the geometry shown in Figure 9.7, we may rewrite this as

$$\mathbf{u}^S(\mathbf{x}, t) = \frac{1}{4\pi\rho\beta^3} (\cos 2\theta \cos \phi \hat{\boldsymbol{\theta}} - \cos \theta \sin \phi \hat{\boldsymbol{\phi}}) \frac{1}{r} \dot{M}_0 \left(t - \frac{r}{\beta} \right), \quad (9.26)$$

where $\hat{\boldsymbol{\theta}}$ and $\hat{\boldsymbol{\phi}}$ are unit Cartesian vectors in the θ and ϕ directions. The resulting S -wave radiation pattern is illustrated in Figure 9.8. There are no nodal planes, but there are nodal points. S -wave polarities generally point toward the T axis and away from the P axis.

The first motions of P waves have long been used to determine earthquake focal mechanisms using the double-couple model. The advantages of this approach, compared to more sophisticated methods of moment tensor inversion, are that only vertical component instruments are required, amplitude calibration is not needed, and the sense of the first P motion (i.e., up or down) can be easily noted from the seismogram at the same time the arrival time is picked, even on analog records. The initial motion of the P wave determines whether the ray left the source in a compressional (upward first motion at a surface receiver) or dilatational quadrant (downward first motion), regardless of sensor type (e.g., displacement, velocity, or acceleration). Ray theory is then used to project the rays from all of the observations back to the angle at which they left the source. The results are plotted on what is termed the *focal sphere*, an imaginary sphere surrounding the source that shows the takeoff angles of the rays. Usually only the lower hemisphere of the focal sphere is plotted, as most rays at teleseismic distances depart downward from the source. (P first motions for upward propagating rays may be plotted on the appropriate opposing point on the lower hemisphere, as the P -wave radiation pattern is symmetric about the origin.)

If enough polarity measurements are plotted, it is possible to divide the focal sphere into compressional and dilatational quadrants. The focal mechanism is then determined by finding two orthogonal planes and their great circle projections onto the focal sphere that separate these quadrants. As discussed above, there is no way to tell from these observations alone which of these planes is the true fault plane and which is the auxiliary fault plane. In the old days, this method was implemented

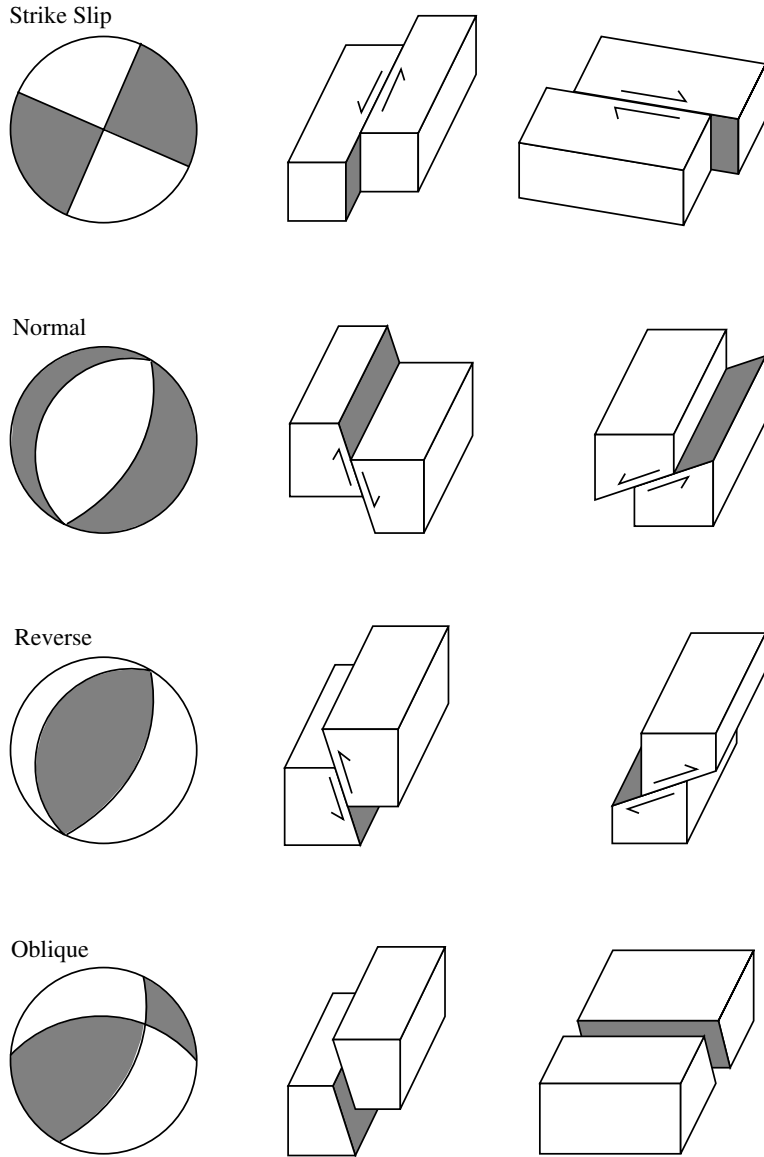


Figure 9.9 Examples of focal spheres and their corresponding fault geometries. The lower half of the focal sphere is plotted to the left, with the compressional quadrants shaded. The block diagrams on the right show the two fault geometries (the primary and auxiliary fault planes) that could have produced the observed radiation pattern.

by hand on special map projections. Today, it is fairly simple to find the focal mechanism using a computer to perform a grid search on the three parameters that define the focal mechanism (strike, dip, rake), directly identifying those solutions that fit the polarity observations most closely.

The focal sphere is also used as a means of displaying focal mechanisms. The lower hemisphere is plotted and the compressional quadrants are shaded to produce the traditional “beach ball” image. This is illustrated in Figure 9.9 for different types of focal mechanisms. In interpreting these plots, remember that the shaded regions

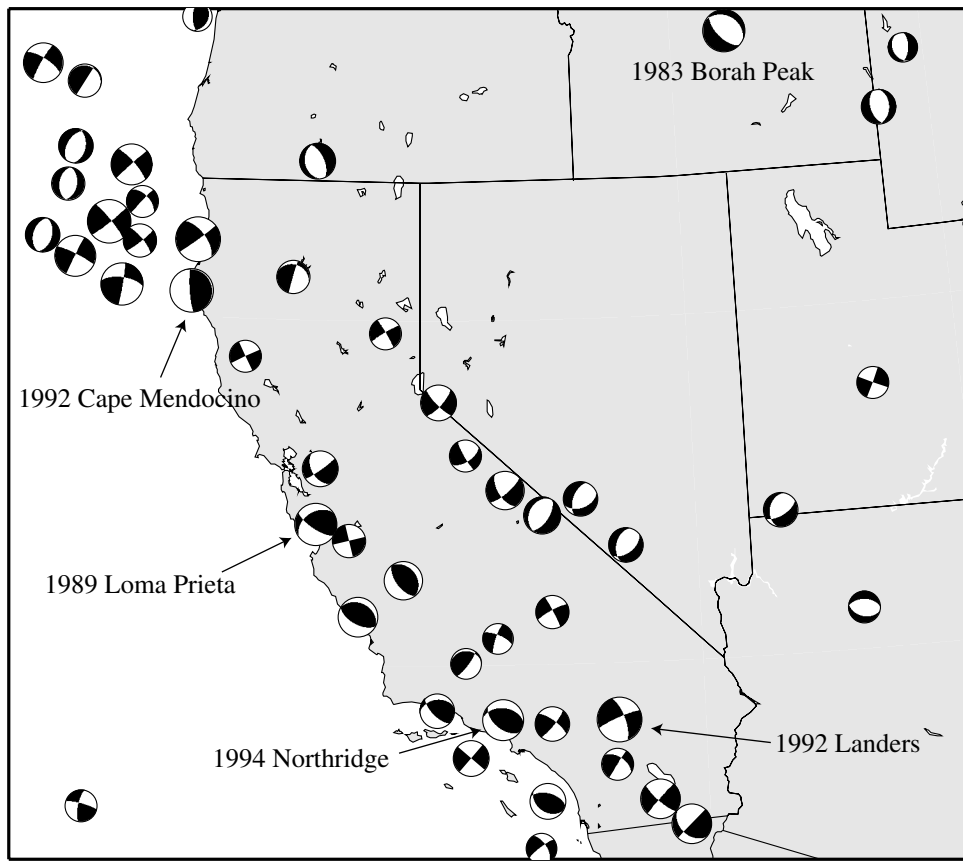


Figure 9.10 Selected focal mechanisms from the Global CMT catalog in the southwestern United States.

represent P waves leaving downward from the source with outward first motions that will produce upward first motions at the receivers, while the unshaded regions will result in downward first motions at the receivers. The tension axis is in the middle of the shaded region; the pressure axis is in the unshaded region. Normal and reverse faulting may be distinguished in beach ball plots by noting if the center of the plot is white or black. If it is white in the middle with black edges, then it represents a normal fault and a probable region of extension, whereas black in the center with white edges indicates a reverse or thrust fault and a likely compressional regime. Examples of strike-slip, normal, and reverse faulting earthquakes are shown in Figure 9.10, which plots global CMT results for the southwestern United States.

Note that the pressure and tension axes give the directions of maximum compression and tension in the Earth only if the fault surface corresponds to a plane of maximum shear. Because this is usually not true, the fault plane solution does not uniquely define the stress tensor orientation (although it does restrict the maximum compression direction to a range of possible angles). However, if multiple focal mechanisms are available at different orientations within a volume in which

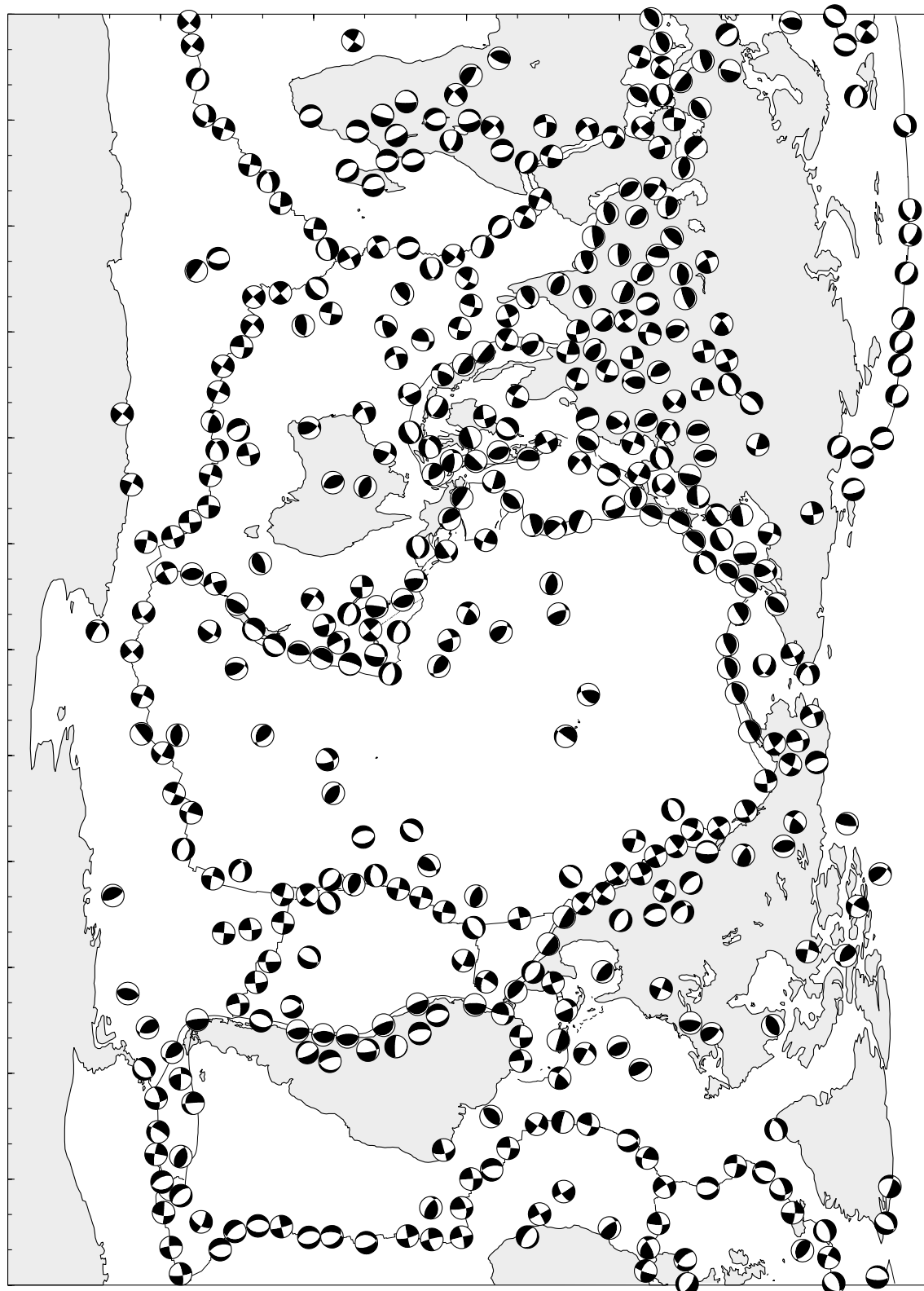


Figure 9.11 Selected focal mechanisms from the Global CMT catalog.

the stress can be assumed homogeneous, then it is possible to estimate the stress tensor orientation (e.g., Gephart and Forsyth, 1984; Michael, 1987). This approach has been used to constrain the principal stress directions in many areas of active seismicity and address questions such as the possible rotation of the stress tensor near active faults.

Focal mechanisms began to be computed from first motions on a routine basis following the establishment of the WWSSN seismic network in the early 1960s. These results confirmed the double-couple theory for earthquake sources and showed that the earthquake mechanisms in different regions were consistent with the emerging theory of plate tectonics. Most earthquakes occur along the boundaries that separate the rigid plates. Strike-slip events are found along active transform faults, such as the San Andreas Fault in California, where the plates are sliding past each other. Reverse fault earthquakes are seen in subduction zones and normal faults in extensional regimes.

The radiation pattern equations presented here are for body waves. Analogous equations are used to describe the generation of surface waves and normal modes. Analyses of longer-period data for source characteristics typically involve a waveform fit and direct inversion for the components of the moment tensor as described earlier. Usually the moment tensor obtained is very close to a pure double couple, and, for convenience, the Global CMT catalog (see Section 9.1 or www.globalcmt.org/CMTsearch.html) provides the strike, dip, and rake for the best-fitting double-couple source. Examples of global focal mechanisms from this catalog between 1976 and 2005 are plotted in Figures 9.10 and 9.11. The complete catalog contains thousands of events; these figures plot the largest earthquakes in each region.

9.3.1 Example: Plotting a focal mechanism

Assume we are given that the strike, dip and rake of an earthquake are 30° , 60° , and 40° respectively and want to sketch the focal mechanism. Figure 9.12 shows how this is done. The left plot is an equal-area lower-hemisphere map of the focal sphere. The numbers around the outside circle show the fault strike in degrees. The circles show fault dip angles with 0° dip (a horizontal fault) along the outer circle and 90° dip (a vertical fault) at the center point. The fault strike of 30° defines point A at 30° and point C at $30 + 180 = 210^\circ$. The fault dip of 60° defines point B, which is on the 60° dip contour on the right side of the line from C to A (recall that faults always dip to the right of the strike direction; see Figure 9.3). The curved line ABC shows the intersection of the fault with the focal sphere. But this is just one of the two fault planes that define the focal mechanism. With a bit of algebra, we can compute the

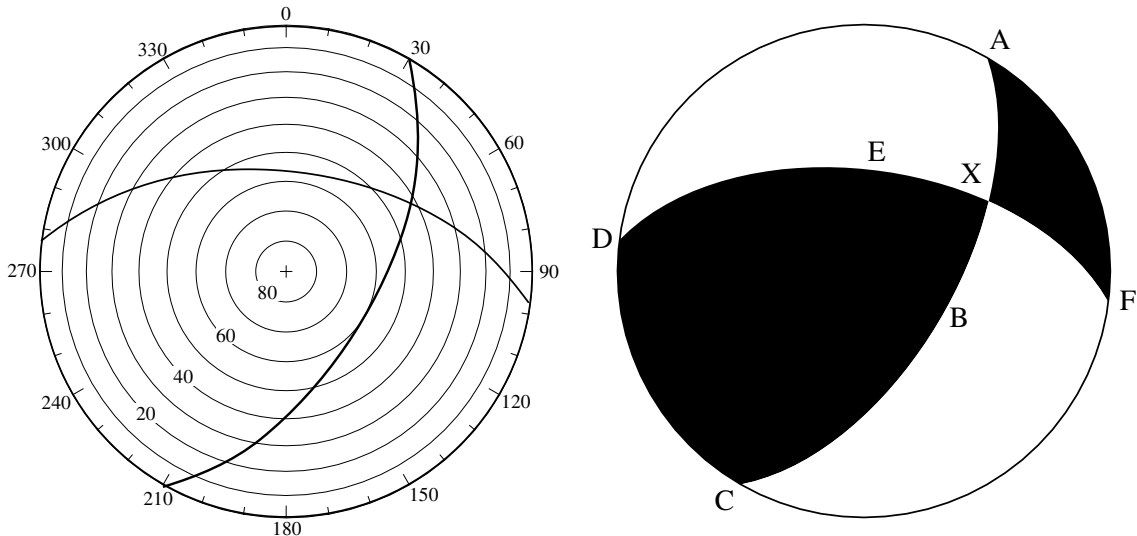


Figure 9.12 An example showing how a focal mechanism is plotted using a lower hemisphere projection.

orientation of the auxiliary plane from the strike, dip, and rake of the first plane. This is described on pp. 228–9 of Stein and Wysession (2002) and is also provided in the subroutine GETAUX in Appendix D. The strike, dip, and rake of this plane are 277.2° , 56.2° and 143.0° and are used to plot curve DEF.

The two curves divide the focal sphere into four parts and the final step is to shade in the correct two quadrants to create the beach ball plot on the right side of Figure 9.12. To get this right, refer again to Figure 9.3 and consider the first fault plane. The rake of 40° gives the angle along the fault plane from the strike direction that the hanging wall side of the fault moves. In lower-hemisphere projections, the hanging wall side is the side that does not include the center point of the plot, i.e., the side to the right of ABC in this example. Because the rake is less than 90° , this side is moving crudely in the direction of point A and thus the area AXF must be in the compressional quadrant and is shaded. The other side of the fault moves in the opposite direction and thus area DEXBC is also shaded. The bottom focal mechanism of Figure 9.9 is close to the orientation of this example and may help in visualizing the slip geometry.

Surface waves in laterally homogeneous media

September 27, 2016

This chapter introduces simple solutions to surface-wave propagation in laterally homogeneous media.

1 Rayleigh waves in a homogenous half space

We consider a Poisson medium as a homogeneous half space, such as $\lambda = \mu$, $\alpha = \sqrt{3}\beta$. The boundary conditions are free traction at the surface and no displacement at $z = \infty$. Love waves do not exist in half spaces so that we focus on Rayleigh waves. The coordinate system is $(\mathbf{e}_x, \mathbf{e}_y, \mathbf{e}_z)$. We write the potentials:

$$\phi = A \exp(ikx + i\eta_\alpha z) \quad (1)$$

$$\psi = B \exp(ikx + i\eta_\beta z) , \quad (2)$$

where ψ is the equivalent of the S_V potential and only the \mathbf{e}_y component is non zero. We satisfy the boundary condition $u_x(z = \infty) = u_z(z = \infty) = 0$ with η_β, η_α taken purely imaginary:

$$\begin{aligned} \eta_\alpha &= i\sqrt{k^2 - \omega^2/\alpha^2} \\ &= ik\sqrt{1 - c^2/\alpha^2} \\ \eta_\beta &= i\sqrt{k^2 - \omega^2/\beta^2} \\ &= ik\sqrt{1 - c^2/\beta^2} \end{aligned} \quad (3)$$

where we anticipate that $c < \beta$ and $c < \alpha$. We have three unknowns, A, B, c (from $k = \omega/c$) and a system of two equations with the traction-free boundary condition at the surface $\sigma_{zz}(z = 0) = 0$ and $\sigma_{zx}(z = 0) = 0$. The displacements and their spatial become for the horizontal component:

$$\begin{aligned} u_x &= \frac{\partial \phi}{\partial x} - \frac{\partial \psi}{\partial z} \\ &= ikA \exp(ikx + i\eta_\alpha z) - i\eta_\beta B \exp(ikx + i\eta_\beta z) \\ \frac{\partial u_x}{\partial x} &= -k^2 A \exp(ikx + i\eta_\alpha z) + k\eta_\beta B \exp(ikx + i\eta_\beta z) \\ \frac{\partial u_x}{\partial z} &= -k\eta_\alpha A \exp(ikx + i\eta_\alpha z) + \eta_\beta^2 B \exp(ikx + i\eta_\beta z) , \end{aligned}$$

and for the vertical component:

$$\begin{aligned} u_z &= \frac{\partial \phi}{\partial z} + \frac{\partial \psi}{\partial x} \\ &= i\eta_\alpha A \exp(ikx + i\eta_\alpha z) + ikB \exp(ikx + i\eta_\beta z) \\ \frac{\partial u_z}{\partial x} &= -k\eta_\alpha A \exp(ikx + i\eta_\alpha z) - k^2 B \exp(ikx + i\eta_\beta z) \\ \frac{\partial u_z}{\partial z} &= -\eta_\alpha^2 A \exp(ikx + i\eta_\alpha z) - k\eta_\beta B \exp(ikx + i\eta_\beta z) \end{aligned}$$

We use Hooke's law to calculate the traction component of the stress tensor:

$$\begin{aligned}
\sigma_{xz}(z) &= \mu \left(\frac{\partial u_x}{\partial z} + \frac{\partial u_z}{\partial x} \right) \\
&= \mu (-k\eta_\alpha A \exp(ikx + i\eta_\alpha z) + \eta_\beta^2 B \exp(ikx + i\eta_\beta z) - k\eta_\alpha A \exp(ikx + i\eta_\alpha z) - k^2 B \exp(ikx + i\eta_\beta z)) \\
&= \mu (-2k\eta_\alpha A \exp(ikx + i\eta_\alpha z) + (\eta_\beta^2 - k^2) B \exp(ikx + i\eta_\beta z)) \\
\sigma_{zz}(z) &= (\lambda + 2\mu) \frac{\partial u_z}{\partial z} + \lambda \frac{\partial u_x}{\partial x} \\
&= 3\mu \frac{\partial u_z}{\partial z} + \mu \frac{\partial u_x}{\partial x} \\
&= 3\mu (-\eta_\alpha^2 A \exp(ikx + i\eta_\alpha z) - k\eta_\beta B \exp(ikx + i\eta_\beta z)) + \mu (-k^2 A \exp(ikx + i\eta_\alpha z) + k\eta_\beta B \exp(ikx + i\eta_\beta z)) \\
&= (-3\mu\eta_\alpha^2 - \mu k^2) A \exp(ikx + i\eta_\alpha z) + (-3\mu k\eta_\beta + \mu k\eta_\beta) B \exp(ikx + i\eta_\beta z) \\
&= \mu(-3\eta_\alpha^2 - k^2) A \exp(ikx + i\eta_\alpha z) - 2\mu k\eta_\beta B \exp(ikx + i\eta_\beta z)
\end{aligned} \tag{4}$$

Taken at the surface, we find that the traction yield to a system of equations for A, B, k , at all x ,

$$\begin{aligned}
0 &= -2k\eta_\alpha A + (\eta_\beta^2 - k^2)B \\
0 &= (-3\eta_\alpha^2 - k^2)A - 2k\eta_\beta B
\end{aligned} \tag{5}$$

This system is satisfied only if the determinant of the system is zero:

$$\begin{aligned}
0 &= -2k\eta_\alpha(-2k\eta_\beta) - (\eta_\beta^2 - k^2)(-3\eta_\alpha^2 - k^2) \\
0 &= -2i\sqrt{1 - c^2/\alpha^2}(-2i\sqrt{1 - c^2/\beta^2}) - (-(1 - c^2/\beta^2) - 1)(3(1 - c^2/\alpha^2) - 1) \\
0 &= -4\sqrt{1 - c^2/\alpha^2}\sqrt{1 - c^2/\beta^2} + (2 - c^2/\beta^2)(2 - 3c^2/\alpha^2)
\end{aligned} \tag{6}$$

This is called a dispersion relation. In a Poisson medium, $\alpha = \sqrt{3}\beta$, and equation 6 becomes

$$4\sqrt{1 - c^2/(3\beta^2)}\sqrt{1 - c^2/\beta^2} = (2 - c^2/\beta^2)(2 - 3c^2/(3\beta^2)), \tag{7}$$

that has four solutions but only one that satisfy $c < \beta$, and you can find the solution $c = 0.92\beta$ using numerical solvers. We can then express the vertical wave numbers :

$$\begin{aligned}
\eta_\alpha &= ik\sqrt{1 - c^2/\alpha^2} \\
&= ik\sqrt{1 - (0.92\beta)^2/(3\beta^2)} \\
&= ik\sqrt{1 - (0.92)^2/3} \\
&= 0.8473ik \\
&= aik \\
\eta_\beta &= ik\sqrt{1 - c^2/\beta^2} \\
&= ik\sqrt{1 - (0.92\beta)^2/\beta^2} \\
&= ik\sqrt{1 - (0.92)^2} \\
&= 0.3919ik \\
&= bik
\end{aligned} \tag{8}$$

And we have the amplitude coefficient:

$$\begin{aligned}
B &= \frac{2k\eta_\alpha}{\eta_\beta^2 - k^2} A \\
&= \frac{2kik\sqrt{1 - c^2/\alpha^2}}{-k^2(1 - c^2/\beta^2) - k^2} A \\
&= -\frac{2i\sqrt{1 - c^2/\alpha^2}}{c^2/\beta^2} A \\
&= -\frac{2ia}{1 + b^2} A \\
&= -1.4673iA
\end{aligned} \tag{9}$$

We can then write the displacements normalized to A :

$$u_x = i \exp(ikx - akz) - b \frac{2ia}{1+b^2} \exp(ikx - bkz) \quad (10)$$

$$= i \left[\exp(-akz) - \frac{2ab}{1+b^2} \exp(-bkz) \right] \exp(ikx) \quad (11)$$

$$= ik [\exp(-0.85kz) - 0.58 \exp(-0.39kz)] \exp(ikx) \quad (11)$$

$$= r_1(z) \exp(ikx) \quad (11)$$

$$u_z = -a \exp(ikx - akz) - i \frac{2ia}{1+b^2} \exp(ikx - bkz) \quad (12)$$

$$= k \left[-a \exp(-akz) + \frac{2a}{1+b^2} \exp(-bkz) \right] \exp(ikx) \quad (12)$$

$$= k [-0.85 \exp(-0.85kz) + 1.47 \exp(-0.39kz)] \exp(ikx) \quad (12)$$

$$= r_2(z) \exp(ikx) \quad (13)$$

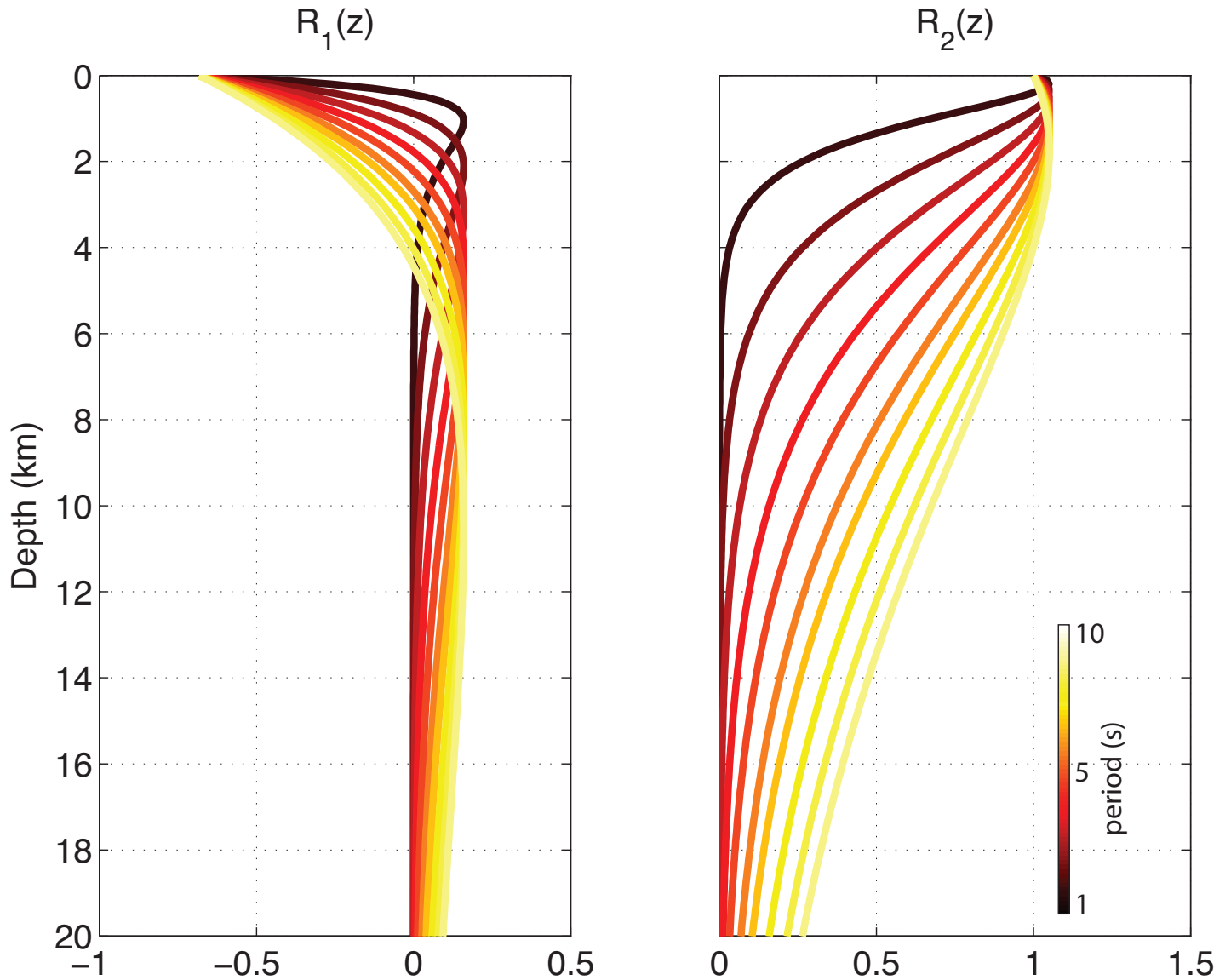
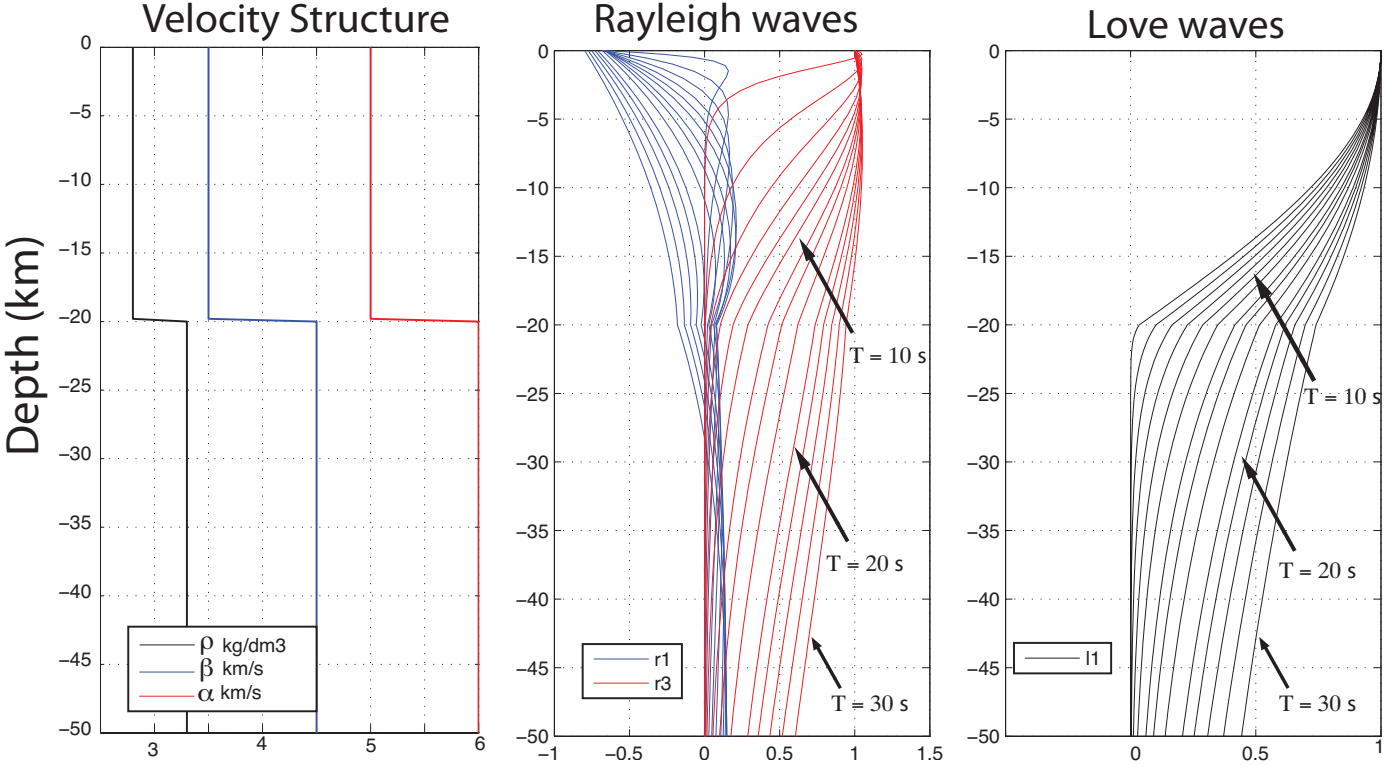


Figure 1: Rayleigh wave displacement eigenfunctions for radial (r_1) and vertical (r_2) components at periods ranging from 1 to 10 seconds. At the surface, Rayleigh waves are retrograde as $r_1 < 0$ and become prograde at frequency-specific depth when $r_2 > 0$.



2 Love waves in a layer over halfspace

Love waves do not exist in half spaces. They are often described as an interference of S_H waves trapped in a layer beneath the air and above a half space with a faster velocity. The top layer of thickness H has density and shear wavespeed ρ_1 and β_1 and the second has a higher density ρ_2 and β_2 . Let's write the Love wave as a sum of an upgoing S_H wave and a downgoing S_H wave in the layer. Let's write

$$u_1(z) = B_1 \exp(-i\eta_1 z) + B_2 \exp(i\eta_1 z) \quad (14)$$

$$u_2(z) = B_3 \exp(-i\eta_2 z), \quad (15)$$

where the vertical slownesses are similar to the Rayleigh wave case, $\eta_2 = k\sqrt{c^2/\beta_2^2 - 1}$ and $\eta_1 = k\sqrt{c^2/\beta_1^2 - 1}$. Note that the Love wave dies at depth ($z \rightarrow \infty$) so that the vertical wavenumber $\eta_2 = ik\sqrt{1 - c^2/\beta_2^2} = i\eta_2^*$ is strictly positive, so that $c < \beta_2$. We use continuity conditions to solve for B_1 , B_2 , B_3 . At the free surface, the traction is zero $\sigma_{yz} = 0$,

$$\sigma_{yz}(0) = \mu_1 \frac{du_1}{dz}(0) \quad (16)$$

$$0 = \mu_1 (-i\eta_1 B_1 + i\eta_1 B_2) \quad (17)$$

$$B_1 = B_2 \quad (18)$$

Traction is continuous at the interface H , such that:

$$\sigma_{yz}(H^+) = \sigma_{yz}(H^-) \quad (19)$$

$$\mu_1 \frac{du_1}{dz}(H^+) = \mu_2 \frac{du_2}{dz}(H^-) \quad (20)$$

$$iB_1 \mu_1 k_1 (-\exp(-i\eta_1 H) + \exp(i\eta_1 H)) = iB_3 \exp(-i\eta_2 H) \quad (21)$$

$$B_1 (\exp(i\eta_1 H) - \exp(-i\eta_1 H)) = B_3 \frac{-\mu_2 \eta_2}{\mu_1 \eta_1} \exp(-i\eta_2 H) \quad (22)$$

Displacement is continuous at the interface H :

$$B_1 (\exp(i\eta_1 H) + \exp(-i\eta_1 H)) = B_3 \exp(-i\eta_2 H) \quad (23)$$

Then we obtain the system of equations:

$$\begin{bmatrix} (\exp(i\eta_1 H) - \exp(-i\eta_1 H)) & -\frac{-\mu_2 \eta_2}{\mu_1 \eta_1} \exp(-i\eta_2 H) \\ (\exp(i\eta_1 H) + \exp(-i\eta_1 H)) & -\exp(-i\eta_2 H) \end{bmatrix} \begin{bmatrix} B_1 \\ B_3 \end{bmatrix} = \begin{bmatrix} 0 \\ 0 \end{bmatrix} \quad (24)$$

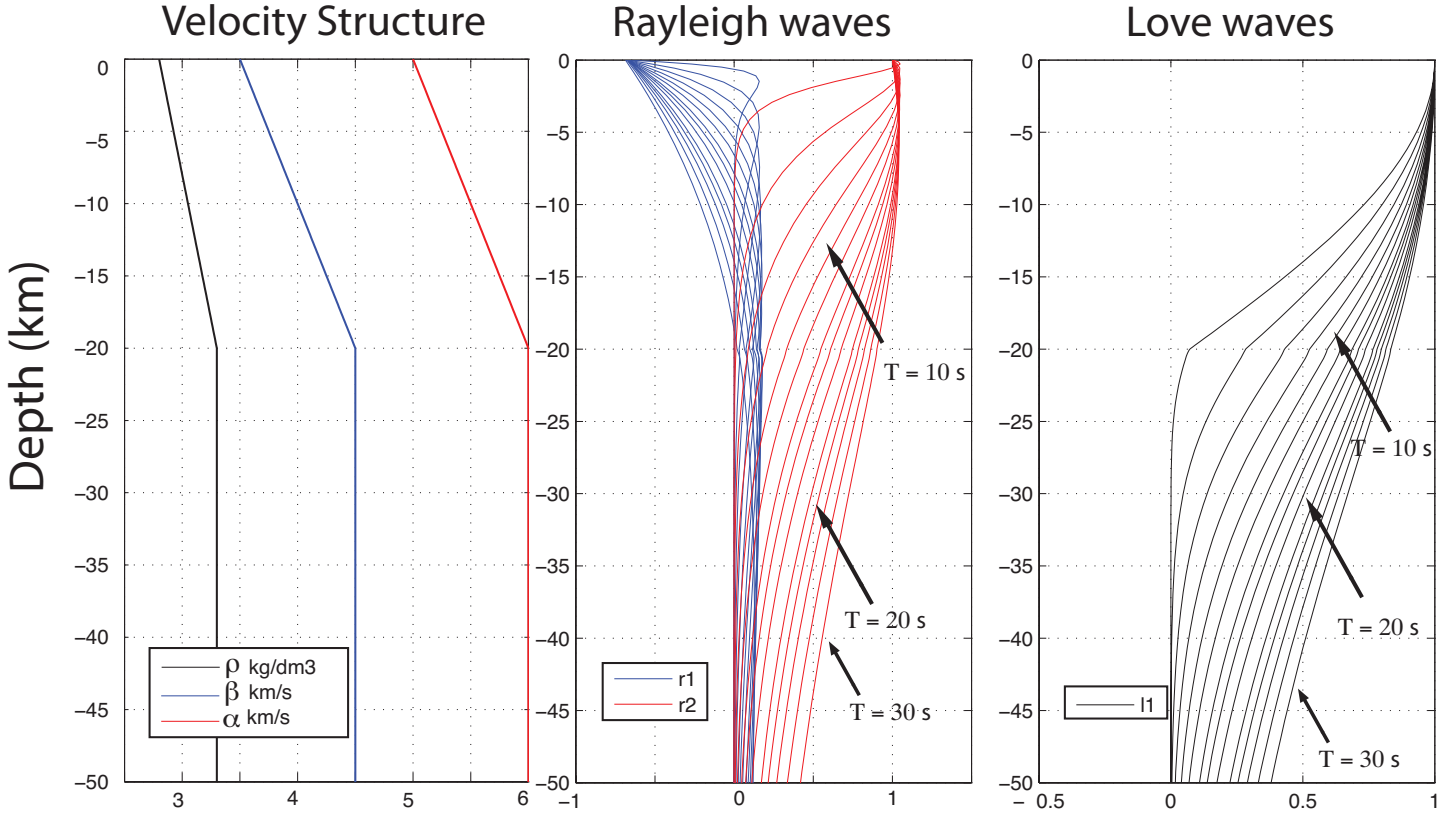


Figure 2: From left to right: Velocity models, Rayleigh and Love wave eigenfunctions at different periods. Long periods eigenfunctions are more sensitive to deeper part of the column than short periods.

$$-\frac{(\exp(i\eta_1 H) - \exp(-i\eta_1 H))}{(\exp(i\eta_1 H) + \exp(-i\eta_1 H))} = \frac{-\mu_2 \eta_2}{\mu_1 \eta_1} \quad (25)$$

$$\tan(\eta_1 H) = \frac{\mu_2 \eta_2}{\mu_1 \eta_1} \quad (26)$$

We explicitly write the dependence of this last result with frequency ω and the unknown phase velocity c :

$$\tan\left(H\omega\sqrt{1/\beta_1^2 - 1/c^2}\right) = \frac{\mu_2}{\mu_1} \frac{\sqrt{1/\beta_2^2 - 1/c^2}}{\sqrt{1/\beta_1^2 - 1/c^2}} \quad (27)$$

We show examples of equation (27) for two periods ($T = 1/2\pi\omega$) in Figure 4(a) for a layer over half space. In this example, the media parameters are $\beta_1 = 3.9$ km/s, $\beta_2 = 4.6$ km/s, $\rho_1 = 2.8$ g/cm³, $\rho_2 = 3.3$ g/cm³. You can find the shear moduli using $\beta = \sqrt{\mu/\rho}$.

3 Surface-wave Green's functions

The elastic medium is characterized by its density ρ and Lamé parameters λ and μ . The compressional and shear wave speeds are α and β . We replace $J_m(kr)$ by $\frac{1}{2} [H_m^{(1)}(kr) + H_m^{(2)}(kr)]$.

Love waves are polarized in the transverse component in the far-field, and in the radial and traverse component in the near field. Rayleigh waves are polarized onto the vertical and radial components. We write the surface-wave Green tensors in the $(\mathbf{e}_r, \mathbf{e}_\theta, \mathbf{e}_z)$ coordinate system for outgoing waves for Love waves:

$$\hat{\mathbf{G}}^L(r, z, \theta, h) = \sum_n \frac{i l_1(z) l_1(h)}{8c_L U_L I_L^1} \begin{bmatrix} \frac{1}{2} [H_0^{(1)}(k_L^n r) + H_2^{(1)}(k_L^n r)] & 0 & \frac{1}{2} [H_0^{(1)}(k_L^n r) - H_2^{(1)}(k_L^n r)] \\ 0 & \frac{1}{2} [H_0^{(1)}(k_L^n r) - H_2^{(1)}(k_L^n r)] & 0 \end{bmatrix}, \quad (28)$$

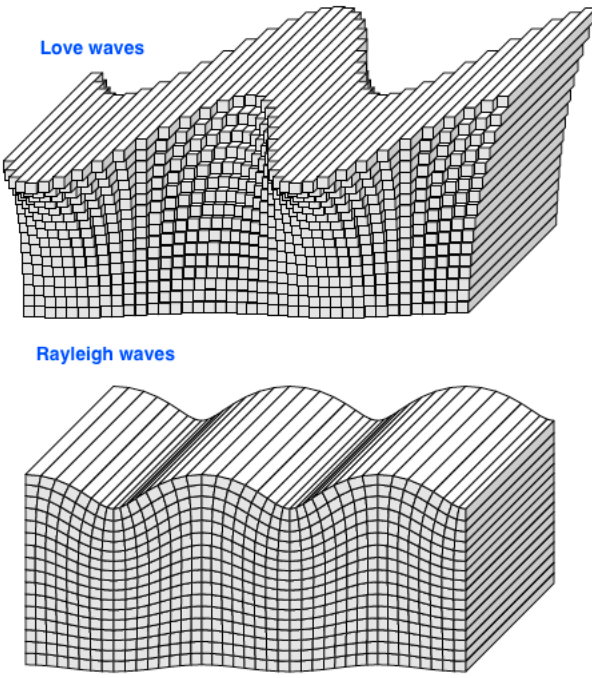


Figure 3: Particle motion at the surface for Love waves (top) and Rayleigh waves (bottom)

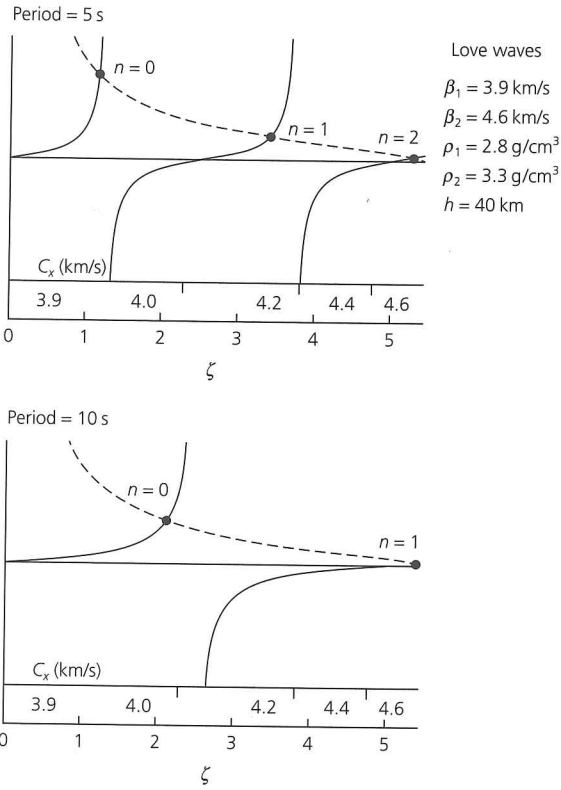
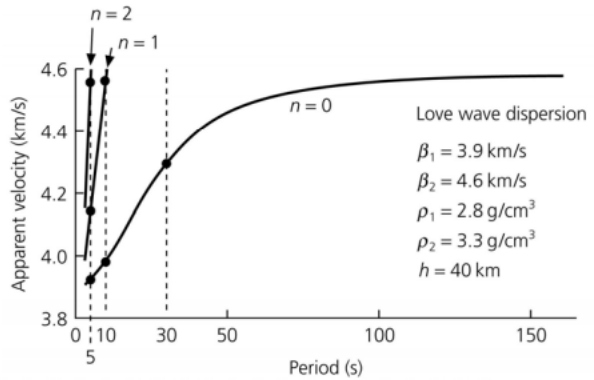


Figure 2.7-8: Dispersion curves for Love waves in a layer over a halfspace.



Dispersion occurs because longer-period waves "see" more of the halfspace, and travel at faster velocities.

- (a) Equation (27) against phase velocity c (noted C_x here) for two periods/frequencies and a given elastic medium (from Stein Stein and Wyssession (2003)) and Wyssession (2003)).

and for Rayleigh waves:

$$\hat{\mathbf{G}}^R(r, z, \theta, h) = \sum_n \frac{i}{8c_R U_R I_R} \begin{bmatrix} \frac{r_1(z)r_1(h)}{2} \left[H_0^{(1)}(k_R^n r) - H_2^{(1)}(k_R^n r) \right] & 0 & r_1(z)r_2(h)H_1^{(1)}(k_R^n r) \\ 0 & \frac{r_1(z)r_1(h)}{2} \left[H_0^{(1)}(k_R^n r) + H_2^{(1)}(k_R^n r) \right] & 0 \\ -r_2(z)r_1(h)H_1^{(1)}(k_R^n r) & 0 & r_2(z)r_2(h)H_0^{(1)}(k_R^n r) \end{bmatrix} \quad (29)$$

where the Love and Rayleigh wave numbers of their n^{th} modes are k_L^n and k_R^n respectively. In the far field, we can take the expansion of the Hankel functions onto exponentials,

$$H_m^{(1)}(kr) \sim \sqrt{\frac{2}{\pi kr}} \exp \left[i \left(kr - \frac{2m+1}{4} \pi \right) \right] \quad (30)$$

In the far-field, we can use the expansions of the Hankel functions to approximate the displacements. When $kr \rightarrow \infty$,

$$\begin{aligned} H_0^{(1)}(kr) + H_2^{(1)}(kr) &\sim -\frac{2}{kr} \exp(ikr + i\pi/4) \sqrt{\frac{2}{\pi kr}} = O \left(\left(\frac{1}{kr} \right)^{3/2} \right) \sim 0 \\ H_0^{(1)}(kr) - H_2^{(1)}(kr) &\sim 2 \exp(ikr - i\pi/4) \sqrt{\frac{2}{\pi kr}} \\ H_0^{(1)}(kr) &\sim \sqrt{\frac{2}{\pi kr}} \exp(ikr - i\pi/4) \\ H_1(1)(kr) &\sim -\sqrt{\frac{2}{\pi kr}} \exp(ikr + i\pi/4) \end{aligned}$$

In the far-field approximation, the Fourier transform of the Green's function become:

$$\hat{\mathbf{G}}^L(z, r, \theta, h) = \sum_n \frac{1}{8c_L^n U_L^n I_1^n} \sqrt{\frac{2}{\pi k_L^n r}} \begin{pmatrix} 0 & 0 & 0 \\ 0 & l_1(z)l_1(h) & 0 \\ 0 & 0 & 0 \end{pmatrix} \exp(i(k_L^n r + \pi/4)), \quad (31)$$

where $l_1^n(z)$ is the n^{th} mode of the Love-wave displacement eigenfunction at depth z , c_L^n the phase velocity, U_L^n the group velocity, k_L^n the wavenumber, $I_1^n = 1/2 \int_0^\infty \rho(z)(l_1^n)^2(z)dz$ is the first energy integral. The Rayleigh-wave Green tensor is

$$\hat{\mathbf{G}}^R(z, r, \theta, h) = \sum_n \frac{1}{8c_R^n U_R^n I_1^n} \sqrt{\frac{2}{\pi k_R^n r}} \begin{pmatrix} r_1^n(z)r_1^n(h) & 0 & -ir_1^n(z)r_2^n(h) \\ 0 & 0 & 0 \\ ir_2^n(z)r_1^n(h) & 0 & r_2^n(z)r_2^n(h) \end{pmatrix} \exp(i(k_R^n r + \pi/4)), \quad (32)$$

4 Surface-wave response to single force point source

The response displacements to a single force point source $\hat{\mathbf{F}}(\omega) = [\hat{F}_r(\omega) \quad \hat{F}_\theta(\omega) \quad \hat{F}_z(\omega)]$ located in $r = 0; z = h$:

$$\begin{aligned} \hat{u}_r(r, \theta, z, h, \omega) &= \frac{r_1(z)}{8c_R U_R I_R^1} [r_1(h)\hat{F}_r(\omega) - ir_2(h)\hat{F}_z(\omega)] \sqrt{\frac{2}{\pi k_R r}} \exp(ik_R r + i\pi/4) \\ \hat{u}_\theta(r, \theta, z, h, \omega) &= \frac{l_1(z)l_1(h)}{8c_L U_L I_L^1} \sqrt{\frac{2}{\pi k_L r}} \hat{F}_\theta(\omega) \exp(ik_L r + i\pi/4) \\ \hat{u}_z(r, \theta, z, h, \omega) &= \frac{r_2(z)}{8c_R U_R I_R^1} [ir_1(h)\hat{F}_r(\omega) + r_2(h)\hat{F}_z(\omega)] \sqrt{\frac{2}{\pi k_R r}} \exp(ik_R r + i\pi/4) \end{aligned} \quad (33)$$

5 Surface-wave response to double couple point source

We rotate the moment tensor of a source \mathbf{M} into the source-receiver axis from the (x, y, z) (north-east-down convention of *Aki and Richards (2002)*) into the (r, θ, z) if the source-receiver azimuth ϕ allows the rotation:

$$\mathbf{R} = \begin{pmatrix} \cos \phi & \sin \phi & 0 \\ -\sin \phi & \cos \phi & 0 \\ 0 & 0 & 1 \end{pmatrix} \quad (34)$$

And we transform the moment tensor $\mathbf{M}^{xyz} = \begin{pmatrix} M_{xx} & M_{xy} & M_{xz} \\ M_{yx} & M_{yy} & M_{yz} \\ M_{zx} & M_{zy} & M_{zz} \end{pmatrix}$ into : $\mathbf{M}^{r\theta z} = \begin{pmatrix} M_{rr} & M_{r\theta} & M_{rz} \\ M_{\theta r} & M_{\theta\theta} & M_{\theta z} \\ M_{zr} & M_{z\theta} & M_{zz} \end{pmatrix}$, using

$$\mathbf{M}^{r\theta z} = \mathbf{R} \quad \mathbf{M}^{xyz} \quad \mathbf{R}^T \quad (35)$$

When doing the matrix multiplication, we find:

$$M_{rr} = \cos^2 \phi M_{xx} + \cos \phi \sin \phi M_{xy} + \cos \phi \sin \phi M_{xz} + \sin^2 \phi M_{yy} \quad (36)$$

$$M_{r\theta} = -\sin \phi \cos \phi M_{xx} + \cos^2 \phi M_{xy} - \sin^2 \phi M_{yx} + \cos \phi \sin \phi M_{yy} \quad (37)$$

$$M_{rz} = \cos \phi M_{xz} + \sin \phi M_{yz} \quad (38)$$

$$M_{\theta\theta} = \sin^2 \phi M_{xx} - \sin \phi \cos \phi M_{xy} - \cos \phi \sin \phi M_{yx} + \cos^2 \phi M_{yy} \quad (39)$$

$$M_{\theta z} = -\sin \phi M_{xz} + \cos \phi M_{yz} \quad (40)$$

$$M_{zr} = \cos \phi M_{zx} + \sin \phi M_{zy} \quad (41)$$

$$M_{\theta z} = -\sin \phi M_{zx} + \cos \phi M_{zy} \quad (42)$$

In the far field, we find that the fundamental mode of surface-wave displacements become:

$$\begin{aligned} \hat{u}_r(r, \theta, z, h, \omega) &= \frac{r_1(z)}{8c_R U_R I_R^1} \sqrt{\frac{2}{\pi k_R r}} [ik_R r_1(h) M_{rr} + ir'_1(h) M_{rz} - ik_R r_2(h) M_{zr} + r'_2(h) M_{zz}] \exp(i(k_R r + \pi/4)) \\ \hat{u}_\theta(r, \theta, z, h, \omega) &= \frac{l_1(z)}{8c_L U_L I_L^1} \sqrt{\frac{2}{\pi k_L r}} [ik_L l_1(h) M_{r\theta} + l'_1(h) M_{z\theta}] \exp(i(k_L r - \pi/4)) \\ \hat{u}_r(r, \theta, z, h, \omega) &= \frac{r_2(z)}{8c_R U_R I_R^1} \sqrt{\frac{2}{\pi k_R r}} [ik_R r_1(h) M_{rr} + ir'_1(h) M_{rz} - ik_R r_2(h) M_{zr} + r'_2(h) M_{zz}] \exp(i(k_R r - \pi/4)) \end{aligned} \quad (43)$$

6 Surface-wave dispersion

Surface-wave tomography depends on dispersion, as expressed by variations in phase velocity c and group velocity U with frequency. These can be related using the energy integrals:

$$c_R = \frac{\omega}{k_R}, \quad c_L = \frac{\omega}{k_L} \quad U_R = \frac{I_2^R + I_3^R/(2k_R)}{c_R I_1^R}, \quad U_L = \frac{I_2}{c_L I_1}, \quad (44)$$

where for Love waves

$$I_1^L = \frac{1}{2} \int_0^\infty \rho l_1^2 dz, \quad I_2^L = \frac{1}{2} \int_0^\infty \mu l_1^2 dz, \quad (45)$$

and for Rayleigh waves

$$\begin{aligned} I_1^R = \frac{1}{2} \int_0^\infty \rho(r_1^2 + r_2^2) dz, \quad I_2^R = \frac{1}{2} \int_0^\infty [(\lambda + 2\mu)r_1^2 + \mu r_2^2] dz, \\ I_3^R = \frac{1}{2} \int_0^\infty \left[\lambda r_1 \frac{dr_2}{dz} - \mu r_2 \frac{dr_1}{dz} \right] dz. \end{aligned} \quad (46)$$